Impact of meteorological and oceanographic conditions on the state of sea ice in Hornsund, Svalbard over 23 years

Vincent Papin[1], Zuzanna M. Swirad[2], A. Malin Johansson[3], and Eirik Malnes[4]

[1]Faculty of Sciences and Technologies, University of Toulon, Toulon, France
[2]Institute of Geophysics, Polish Academy of Sciences, Warsaw, Poland
[3]Department of Physics and Technology, UiT The Arctic University of Norway, Tromsø, Norway
[4]NORCE Research AS, Oslo, Norway

Correspondence: Zuzanna M. Swirad (zswirad@igf.edu.pl) and A. Malin Johansson (malin.johansson@uit.no)

Abstract. The full archive of historical SAR imagery at ~50 m resolution (Envisat ASAR, RADARSAT-2 and Sentinel-1) capturing the Hornsund fjord, Svalbard was used to create an unprecedented set of near-daily binary ice/open water maps over the fjord area for 23 seasons (2002-2025). We observe a general trend with the sea ice season shortening by 2.3 days yr^{-1}, and a gradual decrease in average ice coverage, particularly in the main basin of Hornsund (-1.6% yr^{-1}). The interannual ice condition variability was strongly related to the autumn (October-December) and/or winter (January-March) air temperatures. The length of the sea ice season was shortened by 19.5 days for every 1°C increase in mean autumn air temperature (R^2 = 0.61, $p < 0.05$). Air temperature remained under the freezing point for over 90 days before landfast ice freeze-up. Drift ice was present in the fjord before the freeze-up with an average coverage exceeding 20% 40 days before the landfast ice onset and 26% one day before the ~~landfast ice~~ onset. The landfast ice season break-up period was characterised by a lack of drift ice, and positive air temperatures for over a month. The day of landfast ice freeze-up and break-up overlapped with an average sea ice thickness of 0.33 m and 0.57 m as derived from thermodynamic terms, respectively, suggesting the importance of other processes.

1 Introduction

Awareness of climate change has developed gradually over the decades, as scientific advances have enabled a better understanding of the impact of human activities on the climate. IPCC (2023) showed that the global surface temperature was 1.09°C warmer during the period 2011-2020 compared to 1850-1900, primarily due to the greenhouse gases, dominated by carbon dioxide and methane, partially offset by the cooling effect of aerosols. The Arctic is one of the most affected regions, with a surface temperature increase of more than twice that of the global average, and with some regions experiencing even higher increases (Jansen et al., 2020). Since the beginning of satellite observations in 1978, sea ice coverage in the Arctic has significantly declined, reaching exceptionally low levels in September 2012 (https://nsidc.org/sea-ice-today/sea-ice-tools/charctic-interactive-sea-ice-graph; last access: 16 March 2026). Svalbard is one of the fastest warming regions in the world, with warming in both summer and winter being significant (van der Broek, 2025).

Definicja stylu: Tekst komentarza

The reduction in sea ice cover contributes to the strengthening of surface winds, particularly in autumn and winter, most likely due to the lower surface roughness of open water compared to sea ice (Mioduszewski et al., 2018). This intensification of winds leads to increasing potential fetch and wave height in the region (Casas-Prat and Wang, 2020). These changes result in increased coastal exposure to wave-induced erosion (Zagórski et al., 2015; Herman et al., 2025). For Isfjorden, western Svalbard, the wind direction was found to affect the circulation pattern and hence the ocean surface water temperature (Fraser et al., 2018).

In addition to its environmental impact, sea ice plays a crucial role in Arctic navigation. The extent and thickness of sea ice directly affect the accessibility and safety of maritime routes in the polar region. ~~With the decline of sea ice, previously inaccessible routes, such as the Northern Sea Route and the Northwest Passage, are becoming increasingly navigable during summer months (Smith and Stephenson, 2013). This change has led to increased shipping activity in the Arctic (Pizzolato et al., 2016) and opens new opportunities for commercial shipping and resource exploration.~~ Stocker et al. (2020) investigated the connection between maritime operations and the sea ice variability around Svalbard in 2012-2019, and found a clear correlation between the lack of sea ice and increased maritime operations. Though the behaviour differed between the fishing vessels and the cruise ships in change of location, where cruise ships sought to circumnavigate Spitsbergen and fishing vessels moved northwards.

In coastal Arctic environments, sea ice conditions often differ from those observed in the open ocean due to strong local controls. In sheltered bays landfast ice forms, but the factors influencing the formation and spatial extent of the landfast ice differ regionally and are not fully understood (Itkin et al., 2015). The steep surrounding topography, typical of Arctic fjords, can produce strong local contrasts in wind and near-surface air temperatures, leading to distinct microclimates that influence ice formation processes (Frank et al., 2023). Fjord hydrography is also complex, as oceanic inflows interact with freshwater input from glacier melt and ~~rivers~~river outflow, leading to stratification and circulation patterns that influence ice growth and break-up (Svendsen et al., 2002; Cottier et al., 2010). Beyond their environmental importance, coastal sea ice plays a crucial role for local transportation such as seasonal ice roads for community access, resource exploration and supply delivery (Dong et al., 2025). It also provides temporary protection against wave-driven coastal erosion (Swirad et al., 2026a).

This study focuses on the analysis of fjord ice conditions in Hornsund, Svalbard. The main objectives are threefold: (1) to produce binary ice/open water maps for Hornsund from the early 2000s up to the present day, thereby establishing a consistent long-term record of sea ice conditions; (2) to characterize sea ice and landfast ice seasons in terms of timing, duration and ice coverage; and (3) to identify the atmospheric and oceanic conditions that govern landfast ice freeze-up and break-up in the fjord. Through this approach, the study aims to improve our understanding of local-scale sea ice processes in Hornsund and contribute to a broader comprehension of how Arctic coastal systems respond to ongoing climatic changes.

2 Study area

Hornsund is one of the smallest fjords of Spitsbergen, the largest island of the Svalbard archipelago, located in its south-western part. It opens to the Greenland Sea in the west. The total area of Hornsund is about 320 km^2 with a width of 12 km and a length of 34 km. Its average depth is approximately 100 m, although the maximum depth can reach between 200-250 m in the main basin (Promińska et al., 2018).

The fjord consists of a main basin and several secondary bays, characterized by marine-terminating glaciers (Fig. 1). These bays are Burgerbukta (Vestre and Austre) in the north, Brepollen in the east and Samarinvågen in the south. Brepollen is about 12 km long, connected to the outer fjord by a 2 km wide entrance. Samarinvågen is 7 km long with an entrance 2 km wide, while Burgerbukta is 8 km long and has an entrance of 4 km. A sill at 40-50 m divides Brepollen and Samarinvågen from the main basin, significantly limiting water exchange between the two basins. Similarly there are sills at 25 and 30 m at the entrance to Austre and Vestre Burgerbukta, respectively (Jakacki et al., 2017).

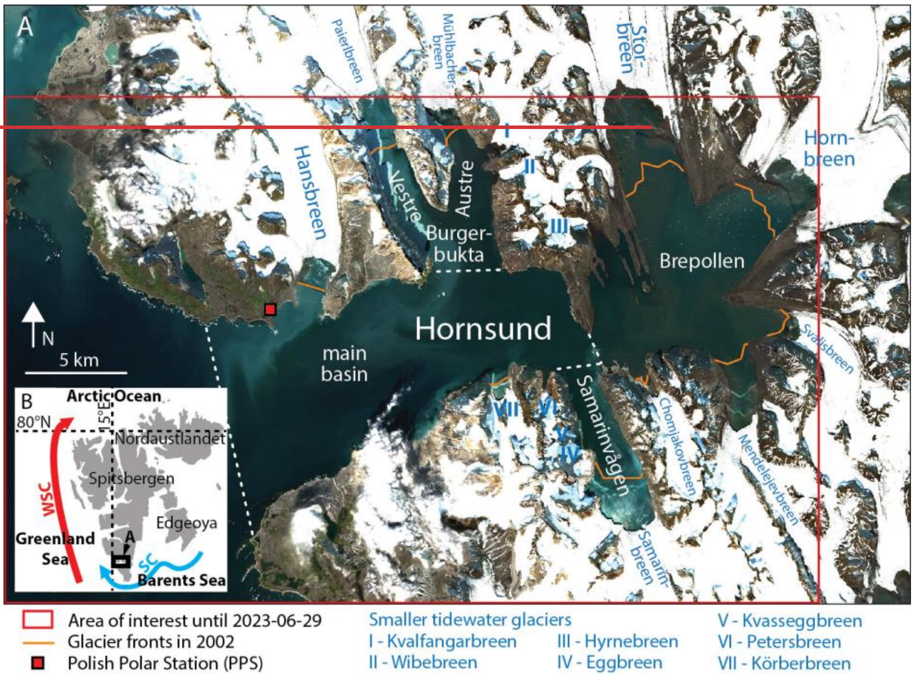

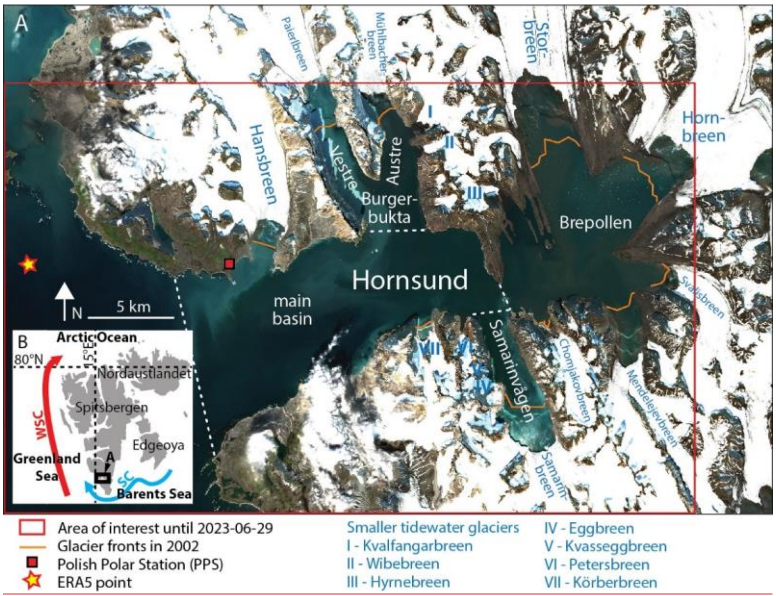

Figure 1. The study area: (a) Hornsund; (b) Svalbard. WSC – West Spitsbergen Current, SC – Sørkapp Current. Background image: Sentinel-2 T33XWF_20250828T120701_TCI_10m scene.

There are 16 tidewater glaciers in Hornsund (Błaszczyk et al., 2023; Fig. 1). Between 2001 and 2010, the glaciers retreated at a rate of 70 m yr^{-1} which is significantly higher than the 45 m yr^{-1} average for Svalbard (Błaszczyk et al., 2013). This glacier retreat has led to an increase in the fjord's surface area, from 188 km^2 in 1936 to 303 km^2 in 2010, as well as in its length, from 24 km in 1936 to 34 km in 2010 (Błaszczyk et al., 2013). ~~Between 2012 and 2017 Hansbreen, Storbreen and Hornbreen lost 11.8, 9.9 and 8.8% total area (Barzycka et al., 2020).~~ Swirad et al. (2026b) calculated a total Hornsund area gain of 30 km^2 between 2011 and 2023 resulting from glacier retreat. ~~The significant increase in glacier retreat in Hornsund has led to a rise in freshwater input to the fjord. During the period 2006-2015, Błaszczyk et al. (2019) estimated an average freshwater input to the Hornsund bays of 2517 ± 82 Mt per year with the main contributions coming from glacier meltwater runoff (39%) and frontal ablation of tidewater glaciers (25%). Secondarily, total precipitation over land (excluding winter snowfall), total precipitation over the fjord area and melting of the snow cover on unglaciated areas accounted for 21, 7 and 8%, respectively (Błaszczyk et al., 2019).~~

Along the west coast of Spitsbergen, outside the fjords, the hydrological conditions and climate are mainly influenced by the West Spitsbergen Current (WSC) carrying warm (3.5-6.0°C) saline (>35 ~~g L^{-1}~~) Atlantic Water (AW) and the Sørkapp Current (SC) carrying cold (-1.5 to 1.5°C) and fresher (34.3-34.8 ~~g L^{-1}~~) Arctic Water (ArW) (Swerpel, 1985; Jakacki et al., 2017; Fig. 1b). The SC carries drift ice from the eastern part of the Svalbard Archipelago (Storfjorden) and the Barents Sea (Jakacki et al., 2017; Korhonen et al., ~~2024; Shulman et al.,~~ 2024). In Hornsund, the presence of AW is relatively limited, however, Strzelewicz et al. (2021) reported an average annual increase of 8% in the volume fraction of AW on the shelf between 1999 and 2020 with this trend becoming especially pronounced during the last decade, a process referred to as Atlantification.

In Hornsund, the water circulation is cyclonic (anticlockwise) with inflow from the southwest and outflow to the northwest. This circulation is mainly governed by tides and shelf currents (Jakacki et al., 2017). The tides are semidiurnal with an amplitude ranging between 0.8 and 1.8 m (Kowalik et al., 2015; Promińska et al., 2018). A statistically significant increase in storm frequency and the number of stormy days per year was observed at the decadal scale outside the fjord (Wojtysiak et al., 2018). The complex configuration of the Hornsund coastline and bathymetry causes strong wave modification through refraction and attenuation (Herman et al., 2019). The significant wave height, *Hs*, varies by location – it reaches 1.2-1.3 m at the fjord's entrance, decreases to 0.5-0.9 m in the central part, and falls below 0.4 m in the inner areas (Swirad et al., 2023b). Since 2006, the seasonal reduction in sea ice cover outside Hornsund has allowed more energetic waves to propagate into the fjord, increasing their impact on coastal zones (Herman et al., 2025).

Herman et al. (2025) suggested that the decline in sea ice cover at the fjord entrance led to changes in the spatial and seasonal distribution of wave energy. Zagórski et al. (2015) demonstrated shoreline retreat of 0.26 m yr^{-1} in Isbjørnhamna, where the Polish Polar Station (PPS) is located (Fig. 1b), between 1960 and 2011. This area ~~has~~ shifted from a coastline formerly influenced by the nearby tidewater Hansbreen and the protection ~~from~~by persistent sea ice and glacier ice to one increasingly exposed to storms and that is undergoing rapid transformation (Zagórski et al., 2015). Additionally, the progressive degradation of permafrost and ground ice due to rising air temperatures reduces the mechanical strength of coastal sediments, making them more vulnerable to erosion (Dobiński and Kasprzak, 2022). Swirad et al. (2026a) observed near-zero net volume beach change in Isbjørnhamna between 2018 and 2025, but they observed existence of an erosional hotspot at the vicinity of the PPS infrastructure, and a net accumulation at the eastern part of the bay.

Between 1979 and 2018, the mean annual air temperature at the PPS meteorological station was -3.7°C, with March being the coldest (-10.2°C) and July – the warmest (4.6°C). Monthly mean temperatures in summer months were relatively stable, typically around 5°C, whereas winter months showed much greater fluctuations with means dropping below -10°C (Wawrzyniak and Osuch, 2020). This strong seasonal variability in winter is attributed to alternating cold, stable anticyclonic subsidence and warmer, cyclonic disturbances (Rinke et al., 2017). The trend in mean annual air temperature over the study period was +1.14°C decade^{-1}, which is more than five times higher than the global average warming rate of +0.17°C decade^{-1} (NOAA, 2025; Wawrzyniak and Osuch, 2020). Dahlke et al (2020) investigated the air temperature change from 1980-2016 for the whole of Svalbard, finding a significant warming over Hornsund for 2010-2016 in January-March compared to the climatological records, with a 1°C decade^{-1} annual warming and a December-February warming of 2.8°C decade^{-1}. Moreover, they found a statistically significant sea ice coverage reduction for the months of February-May for 1998-2016, a statistically significant reduction in May for 1980-1998, though no statistically significant change for 1980-2016. They also observed a reduced impact of wind and ice drift on the total sea ice extent around Svalbard, and that the surface air temperature has a larger impact on the extent.

~~Winds in Hornsund are influenced by the fjord's specific longitudinal shape, its proximity to the coastline and local topography. The prevailing winds are from the east with a mean annual wind speed of 5.5 m s^{-1} recorded~~

between 1983 and 2018. Wind speed shows a clear seasonal variability with average values of 4.0 m s^{-1} in June and 7.1 m s^{-1} in February (Wawrzyniak and Osuch, 2020). Higher wind speed in winter is attributed to the increased frequency of extreme cyclonic events in the Arctic (Rinke et al., 2017).

3 Methods

3.1 Ice mapping

The entire archive of Envisat ASAR, RADARSAT-2 and Sentinel-1 synthetic aperture radar (SAR) imagery that fully covered Hornsund between 2002-10-30 and 2025-08-31 was used in this study (Table 1). The scenes were geocoded with a pixel size of 50 × 50 m and an WGS84, UTM33N extent of X: 499-544 km (901 pixels) and Y: 8531-8559 km (561 pixels) until the end of 2023-06 and X: 498.9-549.1 km (1004 pixels), Y: 8530.9-8564.1 km (664 pixels) starting from 2023-07, a change caused by glacier retreat north- and eastwards beyond the original area of interest (see Fig. 1). The Envisat ASAR was made up of a single channel (HH or VV) radar backscatter sigma nought and the incidence angle GeoTIFF rasters created using GASR software (Larsen et al., 2006). For RADARSAT-2 and Sentinel-1, both HH- and HV-channels radar backscatter sigma nought raster, as well as the incidence angle information were used.

Table 1. Overview of the SAR imagery used in the study.

Sensor	Start date	End date	Number of images	Number of used images	Image frequency (days)	Binary maps URL
Envisat ASAR	2002-10-30	2012-04-07	1826	1061	3.25	https://doi.org/10.1594/PANGAEA.986427 (Papin et al., 2025a)
RADARSAT-2	2012-01-02	2016-03-01	797	638	2.38	https://doi.pangaea.de/10.1594/PANGAEA.969031 (Swirad et al., 2024b)
Sentinel-1	2014-10-14	2023-06-29	2967	2031	1.57	https://doi.org/10.1594/PANGAEA.963167 (Swirad et al., 2023a) Correction (3 images): https://doi.org/10.5281/zenodo.17350297 (Swirad, 2025)
	2023-07-01	2025-08-31	562	443	1.79	https://doi.org/10.1594/PANGAEA.987853 (Papin et al., 2025b)

Tabela sformatowana

— **sformatowano:** Norweski (Bokmål)

— **sformatowano:** Norweski (Bokmål)

— **sformatowano:** Norweski (Bokmål)

— **sformatowano:** Norweski (Bokmål)

— **sformatowano:** Norweski (Bokmål)

— **sformatowano:** Norweski (Bokmål)

— **sformatowano:** Norweski (Bokmål)

— **sformatowano:** Norweski (Bokmål)

— **sformatowano:** Norweski (Bokmål)

— **sformatowano:** Norweski (Bokmål)

— **sformatowano:** Norweski (Bokmål)

— **sformatowano:** Norweski (Bokmål)

— **sformatowano:** Norweski (Bokmål)

— **sformatowano:** Norweski (Bokmål)

— **sformatowano:** Norweski (Bokmål)

A land mask was created using the Norwegian Polar Institute's land shapefile (NPI, 2014). The land mask was updated for each year on July 1st to account for tidewater glacier retreat and, hence, fjord area increase. Finally, a 100 m buffer was applied to exclude the tidal zone from the analysis (Swirad et al., 2024a).

To create binary maps of ice and open water, a segmentation algorithm was used. The algorithm was originally developed by Cristea et al. (2020) for open ocean and adapted to the Svalbard fjord environments by Johansson et al. (2020), and to Hornsund by Swirad et al. (2024a). This algorithm is based on a statistical model that accounts for surface-specific intensity decay with increasing incidence angle, a physical property particularly relevant for flat surfaces such as open water and sea ice (Johansson et al., 2020).

As input, the algorithm requires the incidence angle and one intensity channel, although multiple SAR intensity channels can be used. The HV-channel has lower return power, though is less affected by the wind influence on the water surface which can improve open water vs sea ice separation compared to the HH-channel (Park et al., 2020; Zakhvatkina et al., 2017). However, this channel is limited by a low signal-to-noise ratio (SNR) (Park et al., 2020), and may not always improve the segmentation (Johansson et al., 2020; Zakhvatkina et al., 2017).

The algorithm is initialized with a single segment, which is iteratively optimized using an Expectation-Maximisation algorithm and evaluated with a Pearson-style goodness-of-fit (GOF) test. If the GOF criterion is not met, the segment is split. In cases where multiple segments exist, the least well-fitting segment is selected for division. This process continues until the algorithm reaches an optimal number of segments, defined as the lowest number that provides a sufficiently good fit to the data. A final contextual smoothing step, based on a Markov Random Field (MRF), is applied to improve spatial coherence and ensure simpler visual interpretation.

During the segmentation process, the images were multi-looked 3×3 and log-transformed, and the relevant land mask was used (Johansson et al., 2020; Swirad et al., 2024a). The multi-looking reduced speckle noise and enhanced contrast, while the logarithmic transformation helped approximate a Gaussian distribution of the data (Johansson et al., 2020).

Typically five (range: 3-6) discontinuous segments were automatically mapped. The segments were then manually classified as either "ice" or "open water" based on user experience and assumptions of (i) a better separation between open water and ice in the HV channel and (ii) a higher backscatter value for ice than open water under calm wind conditions (Johansson et al., 2020; Swirad et al., 2024a). Figure 2 shows an example of an original SAR scene, segmentation and classification.

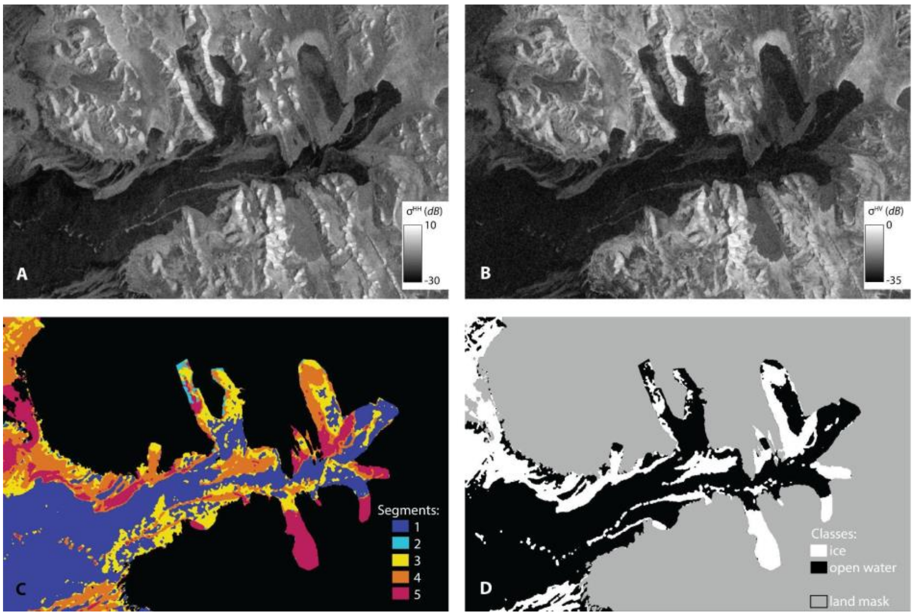

Figure 2. An example of the processing of the Sentinel-1 S1_EWM_20250119_054342_DES_037 scene: (a) HH backscatter intensity, (b) HV backscatter intensity, (c) segmented image, where 1 is the land mask and 2 to 6 are the discontinuous segments, (d) classified image.

Sentinel-1A/B imagery until 2023-06 was processed by Swirad et al. (2024a), RADARSAT-2 imagery was processed by Swirad et al. (2025). The present study contributed by extending the dataset from 11.5 years to nearly 23 years by adding the entire Envisat ASAR archive (Papin et al., 2025a) and Sentinel-1A imagery starting from 2023-07 (Papin et al., 2025b), as well as by fixing erroneously processed Sentinel-1 images on 2015-01-18, 2018-12-25 and 2019-02-12 (Swirad, 2025).

Binary maps were combined into a single time series with a total of 4123 images spanning from 2002-10-30 to 2025-08-31, with an average frequency of 2.02 days. Consistency in ice detection between different sensors was previously verified (Johansson et al., 2020; Swirad et al., 2025). When two images occurred on the same day, RADARSAT-2 was prioritised over Envisat ASAR and Sentinel-1 because of its lower noise floor. Validations of the SAR derived maps were carried out by Johansson et al. (2020) through comparisons with GPS tracks of the landfast ice edge and with manually drawn maps from the Zeppelin observatory in Ny-Ålesund, and by Swirad et al. (2024a) thorough comparisons of the landfast ice edge with 20 temporally and spatially overlapping Sentinel-2 optical images.

3.2 Ice analysis

Binary ice/open water maps were used to characterise spatial and temporal ice conditions in Hornsund. Ice extent and coverage were calculated for the entire fjord as well as for the main basin and three main bays - Burgerbukta, Brepollen and Samarinvågen as delimited in Fig. 1. The coverage was calculated as the ice extent divided by the area of interest, which was updated annually on July 1st based on the landmask extent varied due to glacier front retreat.

The first and last day of the presence of drift and landfast ice inside the fjord were found visually in the SAR intensity images and the binary maps. The sea ice season was defined as the period between the first day of drift ice and landfast ice break-up, while the landfast ice season was delimited by the landfast ice freeze-up and break-up. The length of the sea ice and landfast ice seasons, and the average ice coverage during the sea ice and landfast ice seasons were calculated to identify interannual trends. The ice coverage was calculated for the entire fjord and for its parts – the main basin and the three main bays (Fig. 1) – to identify spatial trends. The seasonal analyses start on September 1st which is defined as the sea ice minimum date (Johansson et al., 2020).

3.3 Meteorological and oceanographic data

Air temperature data from 2002-07-01 to 2025-08-31 come from Vaisala HMP45D and HMP155 probes located 2 m above ground level (12 m a.s.l.), near the main buildings of the PPS, approximately 200 m from the shore. The mean hourly temperature was calculated by averaging hourly min and max values, as these two observations were the only ones available until 2008-06. The mean daily air temperature (T) was calculated by averaging the mean hourly temperature. Mean daily wind speed (WS) was averaged from 1 minute data with measurements performed with different instruments at a height of 10 m above the ground (around 20 m a.s.l.). For days with data gaps, the air temperature and wind speed was taken from the dataset provided by Wawrzyniak and Osuch (2020) for all dates before 2019-01-01, and thereafter linear interpolation of up to seven days was applied.

Daily sea surface temperature (*SST*) and significant wave height (*SWH*) outside Hornsund were obtained from ERA5 reanalysis data (Hersbach et al., 2023) for the position 77°N, 15°E (see Fig. 1) at 12:00 UTC from 2002-07-01 to 2025-08-31. Data gaps, which generally overlap with sea ice concentration values over 30%, were left blank.

T, *WS*, *SST* and *SWH* were subsequently averaged over three months to characterise summer (July-September), autumn (October-December), winter (January-March) and spring (April-June) for each year starting from summer 2002. The summer indicates the preceding summer.

T was also used to calculate the cumulative Freezing Degree Days (FDD) for the period leading to the landfast ice freeze-up and the cumulative Thawing Degree Days (TDD) for the period preceding the landfast ice break-up. FDD represents the sum of the negative temperature on days with degrees below the freezing point of seawater (-1.8°C) starting from Sept 1st, and is defined by the formula given in Equation 1:

$$FDD = \int_0^t (T_f - T(t))\, dt \;\; for \;\; T < T_f \qquad (1)$$

where t is time (days), T_f = -1.8°C is the freezing temperature of seawater ~~(°C),~~, and T is the mean daily air temperature (°C).

Similarly, TDD represents the cumulative sum of degree days with temperatures above 0 °C starting from the landfast ice freeze-up day, and is defined by Equation 2:

$$TDD = \int_0^t T(t)\, dt \;\; for \;\; \mathrm{T} > T_0 \qquad (2)$$

where T_0 is 0°C, and T is the mean daily air temperature (°C).

FDD and TDD were also used to estimate the thermodynamically grown landfast ice thickness. To do so, we first calculated the combined effect of FDD and TDD after Su and Wang (2012) as:

$$\vartheta = FDD - 3 \times TDD \qquad (3)$$

Although FDD and TDD are defined separately in Eqs. 1 and 2, both terms were calculated over the same seasonal period for the ice-thickness estimate so that intermittent freezing and thawing conditions were included through Eq. 3. Here, FDD and TDD were calculated for the same period, starting from the first day with T < -1.8°C and finishing on Aug 31st. Negative ϑ values were replaced by '0'. We then calculated the ice thickness, *SIT* (m) using a formula by Lebedev (1938):

$$SIT = 0.01333 \times \vartheta^{0.58} \qquad (4)$$

The above-mentioned meteorological and oceanographic data were used to (1) characterize conditions during the 23 sea ice seasons and identify long-term trends, (2) find relationships (regression) between forcings and ice conditions (season length and ice coverage), and (3) describe environmental conditions leading to the landfast ice freeze-up and break-up.

4 Results

4.1 Ice conditions over the 23 seasons

The sea ice season began between October and March with the arrival of the drifting ice pack from the southwest, with a mean on December 29th. The landfast ice freeze-up occurred an average 28 days after the first drift ice, between December and March, with a mean on January 26th. The 2004/05 seasonand 2019/20 seasons had the earliest drift ice arrival (October 27th), followed by the 2019/20 season (October 28th), and the and 2015/16 season had the latest onset (March 1st).drift ice arrival. The earliest landfast ice freeze-up occurred in the 2010/11 and 2019/20 (December 18th),, and the latest in the 2015/16 (March 30th). The landfast ice freeze-up occurred on average 28 days after the first drift ice, ranging from 0 (2002/03, 2006/07) to 101 (2005/06) days (Table 2).. Drift ice was present in the fjord until April-July (average until June 1st), while the landfast ice broke up on average 23 days later, in May-July (mean on June 24th). The earliest end of both drift ice and landfast ice presence occurred in 2013/14 (April 9th and May 19th, respectively),, and the latest in 2010/11 (July 20th for both ice types).. The landfast ice break-up (end of both the sea ice and the landfast ice seasons) occurred between 0 (2003/04, 2009/10, 2010/11) and 67 (2024/25) days after the last presence of drift ice (average of 23 days). The sea ice season lasted on average 178 and 150 days, ranging from 105 (respectively, being the shortest in 2015/16) to 249 (and the longest in 2004/05) days. The (sea ice season) or 2010/11 (landfast ice season lasted on average 150 days, ranging from 61 (2015/16) to 215 (2010/11) days) (Table 2).

— **sformatowano:** Kolor czcionki: Czerwony

Table 2. The timing and average ice coverage in Hornsund and its parts over the 23 sea ice seasons from 2002-2025.

Tabela sformatowana

Season	First day with drift ice	Landfast ice freeze-up	Last day with drift ice	Landfast ice break-up
2002/03	2 Jan	2 Jan	9 May	12 Jul
2003/04	13 Nov	7 Jan	30 Jun	30 Jun
2004/05	27 Oct	7 Jan	18 Jun	2 Jul
2005/06	3 Dec	14 Mar	10 May	11 Jun
2006/07	31 Jan	31 Jan	26 Apr	29 Jun
2007/08	8 Jan	17 Feb	3 Jul	8 Jul
2008/09	23 Nov	20 Dec	30 May	5 Jul
2009/10	26 Dec	19 Jan	3 Jul	3 Jul
2010/11	19 Nov	18 Dec	20 Jul	20 Jul
2011/12	11 Dec	17 Feb	6 Jun	11 Jun
2012/13	8 Feb	11 Feb	4 Jun	21 Jun
2013/14	2 Jan	12 Jan	9 Apr	19 May
2014/15	29 Dec	27 Jan	13 Jun	7 Jul
2015/16	15 Feb	30 Mar	26 May	29 May
2016/17	1 Mar	7 Mar	18 May	18 Jun
2017/18	30 Dec	29 Jan	23 May	4 Jun
2018/19	25 Jan	12 Feb	3 Jun	18 Jun
2019/20	28 Oct	18 Dec	26 May	29 Jun
2020/21	2 Feb	4 Feb	8 Jun	24 Jun
2021/22	3 Dec	28 Dec	23 May	22 Jun
2022/23	11 Feb	21 Feb	24 May	12 Jun
2023/24	1 Jan	4 Jan	29 Jun	4 Jul
2024/25	10 Jan	12 Jan	30 Apr	6 Jul
Mean	**29 Dec**	**26 Jan**	**1 Jun**	**24 Jun**

There was a gradual decrease in the length of the driftsea ice and landfast ice seasons of 2.34 and 0.66 days yr^{-1}, respectively, though the relationships are weak and statistically insignificant (Fig. 3a).

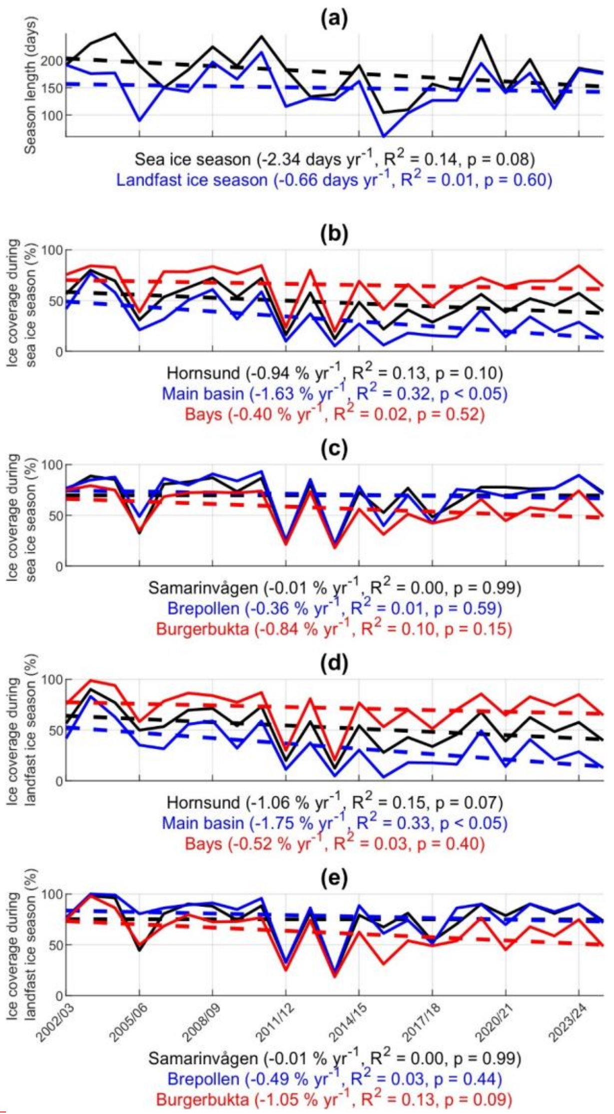

.

Figure 3. Time series of ice season parameters in Hornsund over the 23 seasons from 2002–2025: (a) the length of the sea ice season and the landfast ice season; average ice coverage during the sea ice season (b) for the parts of Hornsund, and (c) for individual bays; average ice coverage during the landfast ice season (d) for the parts of Hornsund, and (d) for individual bays.

The average ice coverage in Hornsund was 48% during the entire sea ice season, but it was higher in the bays (66%) and lower in the main basin (31%). Earlier seasons (2002/03 to 2010/11) experienced higher ice coverage (≥ 53%) with the exception of the 2005/06 (31%). The maximum overall ice coverage was reached in 2003/04 (80% in Hornsund, 77% in the main basin and 84% in the bays). From 2011/12, the average ice coverage was more variable for from year to year, ranging from 12% in 2013/14 to 57% in 2023/24 (Fig. 4).. Of the bays, Brepollen was characterized by the highest average ice coverage during the sea ice season (70%), followed by Samarinvågen (69~~%), which had higher ice coverage than Brepollen in some seasons. Meanwhile,~~%) and Burgerbukta ~~had~~(57%). Similar trends characterised the ~~lowest average ice coverage during the sea~~landfast ice season~~ (57%)~~.. There was a statistically-significant negative trend in ice coverage in the main basin during the sea ice season (-1.63% yr^{-1}, $R^2 = 0.32$, $p < 0.05$~~). The long-term trends of the entire fjord and the bays were weak and non-significant (Fig. 3b,c~~) and during the landfast ice season ((-1.75% yr^{-1}, $R^2 = 0.33$, $p < 0.05$) (Fig. 3).

— **sformatowano:** Czcionka: Nie Pogrubienie, Nie Wyróżnienie

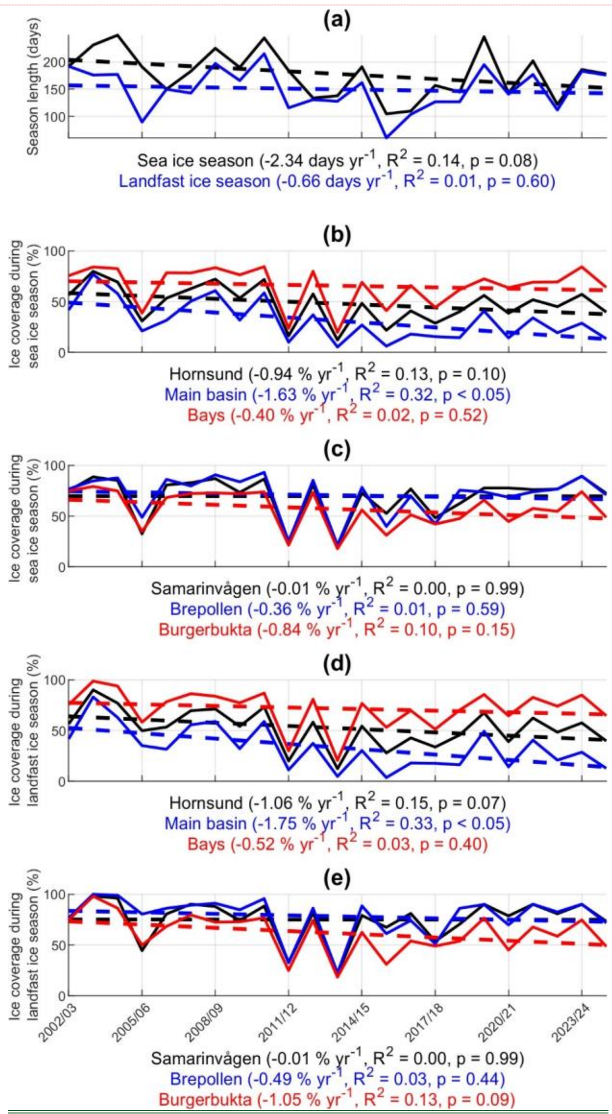

Figure 3. Time series of ice season parameters in Hornsund over the 23 seasons from 2002-2025: (a) the length of the sea ice season and the landfast ice season; average ice coverage during the sea ice season (b) for the parts of Hornsund,

and (c) for individual bays; average ice coverage during the landfast ~~The ice coverage during the landfast ice season followed the same interannual and spatial pattern as for the sea ice season. The average coverage was, however, higher by 4, 2 and 6% for Hornsund, main basin and the bays, respectively. The results of linear regression showed a statistically-significant negative trend for the ice coverage in the main basin (-1.75% yr^{-1}, $R^2 = 0.33$, $p < 0.05$), while other areas exhibited weak non-significant trends (Fig. 3d, e).~~

~~During~~**ice season (d) for the parts of Hornsund, and (e) for individual bays.**

On the day of the landfast ice freeze-up, the drift ice was typically present outside the fjord and in the main basin while landfast ice mostly ~~formed~~started forming in Samarinvågen and southern Brepollen (Fig. 4a). During the landfast ice break-up the main basin was usually ice-free while the last landfast ice was present in Vestre Burgerbukta, northern Brepollen and depths of Samarinvågen (Fig. 4b).

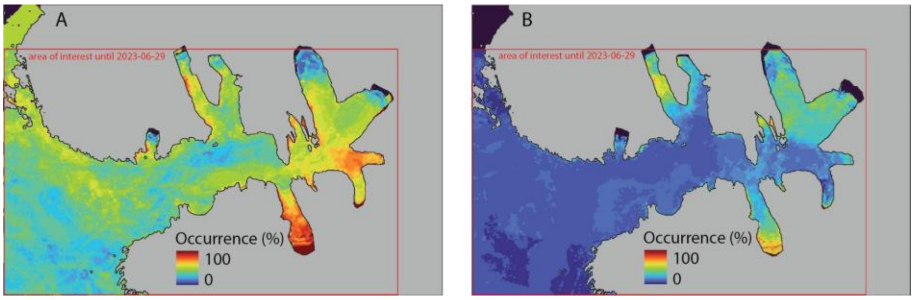

Figure 4. ~~**Spatial occurrence**~~**Mean distribution of ice on the (a) freeze-up and (b) break-up of the landfast ice in Hornsund over the 23 seasons from 2002–2025.**

4.2 Meteorological and oceanographic conditions

T averaged over the 23 seasons was 4.2°C in summer, -3.6°C in autumn, -8.0°C in winter and -1.7°C in spring. The first negative air temperatures in the fjord occurred between September and November, with the earliest recorded on September 7th (2002) and the latest on November 1st (2016). The last day of negative air temperature occurred between May and June, with the earliest on May 20th (2016 and 2022) and the latest on June 12th (2010). ~~Over the 23 seasons, the minimum *T* of -28.1°C was recorded on January 13th, 2004, and the maximum of 12.0°C on July 25th, 2020.~~
WS was characterised by a high variability at a daily timescale. Seasonally, stronger winds were observed in winter (6.8 m s^{-1}) and autumn (6.2 m s^{-1}), compared to summer (4.6 m s^{-1}) and spring (5.4 m s^{-1}). ~~The maximum *WS* of 20.3 m s^{-1} was recorded on January 10th, 2019, while *WS* of 0 m s^{-1} occurred on 10 days during the study period.~~
SST was the lowest in winter (0.3°C) and the highest in summer (4.2°C). It averaged 1.2°C in autumn and 0.9°C in spring. The first negative *SST* values occurred between October and March, with the earliest recorded on October 17th (2005) and the latest on March 28th (2017). The last day with negative *SST* occurred between April and July, with the earliest on April 1st (2006) and the latest on July 7th (2004). ~~Over the 23 seasons, the lowest *SST* of -1.8°C was recorded on April 27th, 2013, and the highest of 7.4°C on August 14th and 15th, 2002.~~ *SWH* was the

highest in winter (2.1 m), followed by autumn (1.8 m), spring (1.1 m), and summer (1.1 m). The largest *SWH* of 7.9 m was observed on February 7th, 2025, and the lowest of 0.2 m occurred on July 7th, 2003, May 19th, 2020, and May 4th, 2021.

There was a strongwere four statistically-significant trend of($p < 0.05$) long-term seasonal trends in our dataset: increasing T_{summer} over the analysed 23 seasons (+0.08°C yr^{-1}, $R^2 = 0.59$, $p < 0.05$). The other seasons also experienced a gradual *T* increase, but relationships are weak and non-significant. *WS* increased in summer), increasing WS_{summer} (+0.04 m s^{-1} yr^{-1}, $R^2 = 0.32$, $p < 0.05$) and decreased in winter), decreasing WS_{winter} (-0.04 m s^{-1} yr^{-1}, $R^2 = 0.29$, $p < 0.05$). Trends in autumn and spring were weak and non-significant. *SST* trends were generally weaker than those observed for *T* with the summer increase of +0.05°C yr^{-1} ($R^2 = 0.17$, $p = 0.05$) and a negligible and non-significant trends in other seasons. *SWH* exhibited a limited long-term changes across seasons with the only statistically-significant positive trend in spring) and increasing SWH_{spring} (+0.01 m yr^{-1}, $R^2 = 0.21$, $p < 0.05$) (Fig. 5).

sformatowano: Czcionka: Kursywa

sformatowano: Czcionka: Kursywa

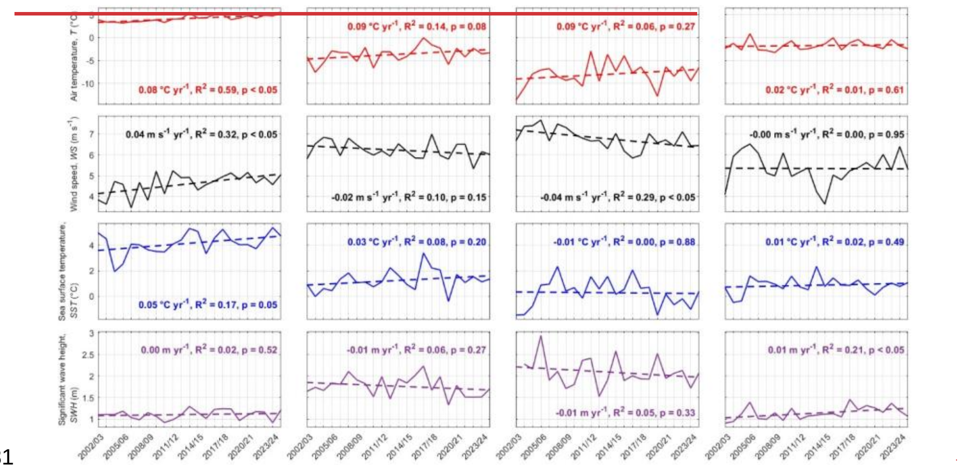

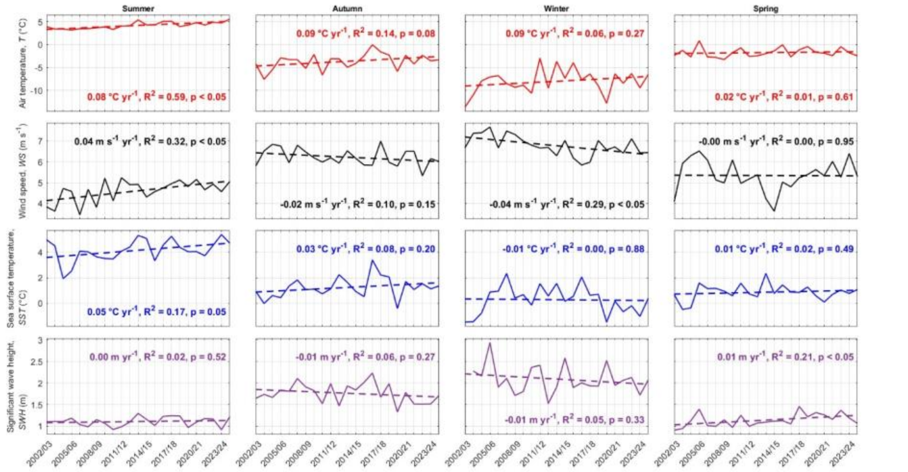

Figure 5. Seasonal averages of meteorological and oceanographic parameters in Hornsund for the 23 seasons from 2002-2025.

4.3 Relationships between environmental conditions and the ice-season parameters

In general, longer and icier seasons were associated with colder autumns and winters. The 2003/04 season had the highest ice coverage in Hornsund (80% during the sea ice and 90% during the landfast ice season), the lowest T_{autumn} (-7.6°C), the third lowest T_{winter} (-11.0°C), one of the highest WS_{winter} (7.4 m s^{-1}), the lowest SST_{spring} (-0.5°C). The 2004/05 season had the longest sea ice season (249 days), the second-highest ice coverage in the fjord during the landfast ice season (77%), ~~and~~ the earliest first drift ice (October 27th~~). It was characterized by~~), the lowest SST_{summer} (1.9°C) and one of the highest WS_{winter} (7.4 m s^{-1}). The 2010/11 season had the longest landfast ice season (215 days) related to the earliest landfast ice freeze-up (December 18th) and the latest landfast ice break-up (July 20th). T_{summer} was the second lowest (3.3°C), and T_{winter} was one of the lowest (-10.6°C). The 2019/20 season also had the earliest landfast ice onset (December 18th). Additionally, it had also one of the largest ice coverages, particularly in the bays (72% during sea ice season and 85% during landfast ice season). It was characterized by the lowest SST_{winter} (-1.5°C), the lowest SST_{autumn} (-0.4°C), and the lowest SWH_{autumn} (1.3 m).

The 2013/14 season had the lowest ice coverage in Hornsund (12% during both the sea ice and the landfast ice seasons) and its bays (20% during the sea ice and 21% during the landfast ice season), and the earliest end of the landfast ice season (May 19th). This season had the highest SST_{spring} (2.3°C), the highest SWH_{summer} (1.3 m) and the second highest T_{winter} (-3.7°C). The 2015/16 season had the shortest sea ice and landfast ice seasons (105 and 61 days, respectively), the latest landfast ice onset (March 30th), and the lowest ice coverage in the main basin (3.6%). This season was marked by the second highest T_{spring} (-3.2°C). The 2016/17 season had the latest occurrence of the first drift ice (March 1st). It was also characterized by the highest T_{autumn} (-0.01°C) and the lowest WS_{winter} (5.9 m s^{-1}) and it recorded the highest SST_{autumn} (3.4°C), as well as the highest SWH_{autumn} (2.2 m).

Strong ($R^2 \geq 0.48$) statistically-significant ($p < 0.05$) negative relationships exist between T_{autumn} or T_{winter} and all considered characteristics of sea ice and landfast ice seasons: season length and ice coverage in Hornsund, the main basin and the bays (Fig. 6). The length of the sea ice season decreased by 19.5 days per 1°C increase in T_{autumn} (R^2 = (Fig. 6). 0.61, $p < 0.05$), while the length of the landfast ice season decreased by 10.1 days per 1°C increase in T_{winter} ($R^2 = 0.48$, $p < 0.05$). The average ice coverage in the main basin during the sea ice season decreased by 8.2% per 1°C increase in T_{autumn} ($R^2 = 0.52$, $p < 0.05$). The ice coverage the entire fjord and in the bays during the sea ice season depended on the T_{winter} with trends of -5.3% per 1°C ($R^2 = 0.59$, $p < 0.05$) and -5.4% per 1°C ($R^2 = 0.55$, $p < 0.05$), respectively. Similar patterns were observed for the ice coverage during the landfast ice season with the respective trends of -5.4% per 1°C ($R^2 = 0.58$, $p < 0.05$), 8.7% per 1°C ($R^2 = 0.52$, $p < 0.05$) and 5.4% per 1°C ($R^2 = 0.57$, $p < 0.05$) in Hornsund, the main basin and the bays, respectively (Fig. 6).

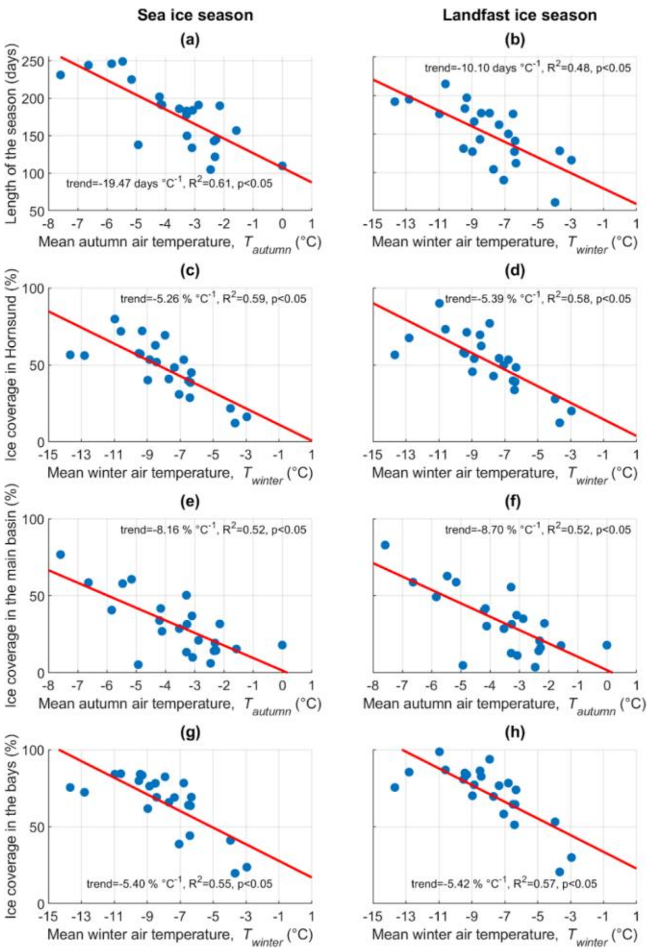

Figure 6. Linear correlations between the highest-correlation environmental driver (mean autumn or winter air temperature) and the ice-season parameters over the 23 seasons from 2002-2025: (a-b) length of the season; (c-d) average ice coverage in Hornsund; (e-f) average ice coverage in the main basin; (g-h) average ice coverage in the bays. The left panel represents the sea ice season and the right panel – the landfast ice season.

Figure 7 shows results of the linear stepwise regression models relating environmental drivers to key parameters of the sea ice season (left panel) and the landfast ice season (right panel). The 16 drivers (*T*, *WS*, *SST* and *SWH* over summer, autumn, winter and spring) were considered. For all ice-season parameters using multiple predictors improved the fit (adjusted $R^2 \geq 0.73$, $p < 0.05$ for seven out of eight parameters) compared to a single predictor (Fig. 7). T_{winter} appears in all eight ice-season parameters and is consistently associated with a negative relationship. T_{autumn} and T_{spring} explain four parameters, and in all cases their relationship with the ice season parameters is negative. T_{summer} represents an outlier, as it appears only in the equation for the average ice coverage in the bays during the sea ice season, where it shows a positive relationship. WS_{summer} appears in six cases and is consistently associated with a negative relationship. In contrast, WS_{winter} is present in five of the ice-season parameters and always shows a positive relationship. WS_{autumn} appears in three cases, with a positive relationship in two of them (the length of the sea ice season and the average ice coverage in the main basin during the landfast ice season), and a negative relationship in the average ice coverage in the bays during the sea ice season. WS_{spring} does not appear in any of the equations. SST_{spring} is present in six out of eight cases and is consistently associated with a negative relationship. SST_{winter}, which appears in the equations for the average ice coverage in the main basin during both the sea ice and landfast ice seasons, shows a positive relationship. SST_{autumn} also exhibits a positive relationship for the average ice coverage in the main basin and in the bays during the sea ice season, but a negative relationship for the length of the sea ice season. SST_{summer}, which is present in half of the cases, always has a negative correlation. SWH_{summer} and SWH_{autumn} each appear in two cases and are consistently associated with a negative relationship. SWH_{winter} is present in three cases, showing a negative relationship in two of them (the average ice coverage in Hornsund and in the bays during the sea ice season), and a positive relationship for the length of the sea ice season. Finally, SWH_{spring} does not appear in any of the equations (Table 3).

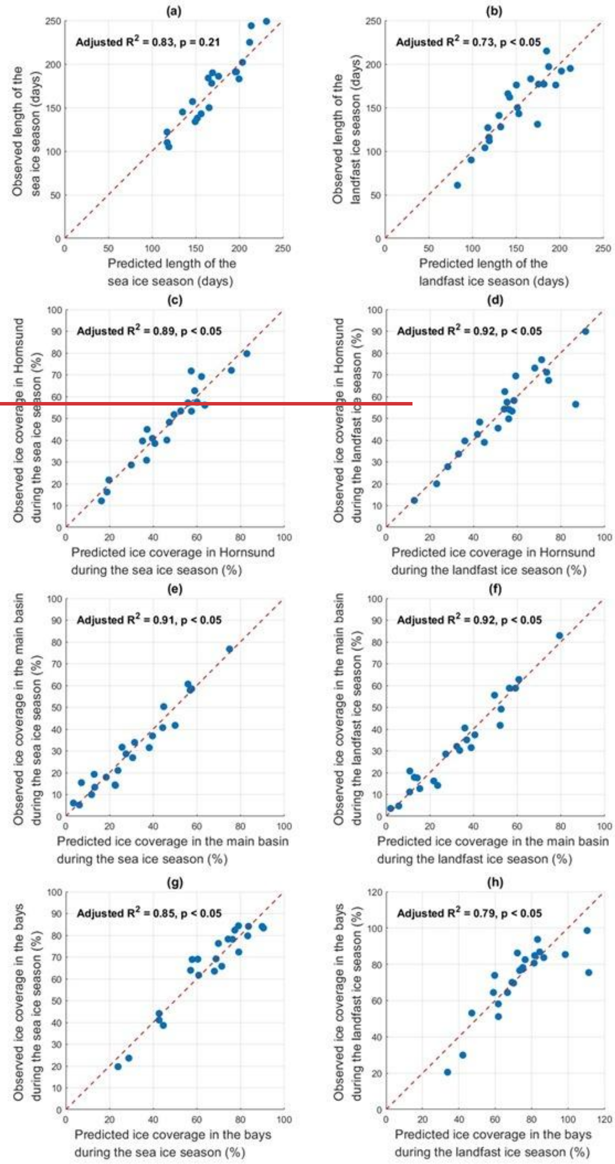

~~**Figure 7. Results of the stepwise regression between environmental drivers and ice-season parameters over the 23 seasons from 2002-2025: (a-b) length of the season; (c-d) average ice coverage in Hornsund; (e-f) average ice coverage in the main basin; (g-h) average ice coverage in the bays. The left panel represents the sea ice season and the right panel – the landfast ice season.**~~

Stepwise linear regression relating environmental drivers to ice season parameters showed that using multiple predictors improved the fit (adjusted $R^2 \geq 0.73$, $p < 0.05$ for seven out of eight parameters) compared to a single predictor (Fig. 6 vs Table 3). Predictors showing negative correlations with multiple ice season parameters are T_{winter}, T_{autumn}, T_{spring}, WS_{summer}, SST_{spring}, SST_{summer}, SWH_{summer}, SWH_{autumn} and SWH_{winter}. Conversely, a positive correlation links ice season parameters to WS_{winter}, WS_{autumn}, SST_{winter} and SST_{autumn} (Table 3).

Table 3. Stepwise regression models of the ice-season parameters in Hornsund over the 23 seasons from 2002-2025.

Ice-season parameter	Best-fit model	Adjusted R^2	*p*-value
Length of the sea ice season	$-135.76 - 5.09 \times T_{autumn} - 7.14 \times T_{winter} - 12.74 \times T_{spring} + 26.16 \times WS_{autumn} - 18.63 \times SST_{autumn} + 37.28 \times SWH_{winter}$	0.83	0.21
Average ice coverage in Hornsund during the sea ice season	$9.98 - 4.43 \times T_{winter} - 2.60 \times T_{spring} - 10.72 \times WS_{summer} + 10.45 \times WS_{winter} - 5.07 \times SST_{spring} - 8.51 \times SWH_{winter}$	0.89	7.04×10^{-6}
Average ice coverage in the main basin during the sea ice season	$23.63 - 6.31 \times T_{autumn} - 3.11 \times T_{winter} - 10.22 \times WS_{summer} + 5.82 \times WS_{winter} - 3.90 \times SST_{summer} + 7.23 \times SST_{autumn} + 3.30 \times SST_{winter} - 9.09 \times SST_{spring} - 16.42 \times SWH_{summer}$	0.91	4.80×10^{-4}
Average ice coverage in the bays during the sea ice season	$66.60 + 15.83 \times T_{summer} - 5.11 \times T_{winter} - 17.75 \times WS_{summer} - 5.56 \times WS_{autumn} + 17.79 \times WS_{winter} - 7.09 \times SST_{summer} + 8.37 \times SST_{autumn} - 7.12 \times SST_{spring} - 56.25 \times SWH_{summer} - 11.61 \times SWH_{winter}$	0.85	0.03
Length of the landfast ice season	$108.31 - 8.51 \times T_{autumn} - 5.97 \times T_{winter} - 14.18 \times T_{spring} - 34.71 \times SWH_{autumn}$	0.73	8.68×10^{-3}
Average ice coverage in Hornsund during the landfast ice season	$25.92 - 4.70 \times T_{winter} - 10.82 \times WS_{summer} + 8.32 \times WS_{winter} - 2.54 \times SST_{summer} - 6.84 \times SST_{spring}$	0.92	4.48×10^{-7}
Average ice coverage in the main basin during the landfast ice season	$-3.08 - 4.43 \times T_{autumn} - 4.13 \times T_{winter} - 10.75 \times WS_{summer} + 5.84 \times WS_{autumn} + 6.24 \times WS_{winter} - 3.23 \times SST_{summer} + 7.42 \times SST_{winter} - 10.11 \times SST_{spring} - 12.16 \times SWH_{autumn}$	0.92	3.66×10^{-3}
Average ice coverage in the bays during the landfast ice season	$84.21 - 5.16 \times T_{winter} - 9.58 \times WS_{summer} - 9.51 \times SST_{spring}$	0.79	3.00×10^{-5}

Tabela sformatowana

4.4 Conditions leading to the landfast ice freeze-up and break-up

In the period leading to the onset of landfast ice, *T* gradually decreased (-0.1°C day^{-1}, $R^2 = 0.81$, $p < 0.05$) with the average below the sea water freezing point for > 90 days (Fig. ~~8a~~7a). The 2009/10 season had the highest mean *T* (-3.1°C), while the 2003/04 season had the lowest mean *T* during this 90-days period (-8.2°C). The drift ice appeared on average 28 days earlier, ranging from 0 (2002/03 and 2006/07) and 101 days (2005/06). Ice coverage during the period between first day with drift ice and the first day with landfast ice averaged 21% with the minimum of 0% in 2009/10 (drift ice was present outside the fjord and no imagery was available between December 26th and January 19th for a better assessment) and the maximum of 85% in 2008/09 (Table 4). Ice coverage generally remained low during the early part, followed by an increase as the landfast ice freeze-up approached. The timing varied from year to year but 40 days before the ~~landfast ice~~ freeze-up the average ice coverage exceeded 20%. The average coverage of 26% characterised the day before and 46% the freeze-up day (Fig. ~~9~~8). The period leading to the landfast ice freeze-up was also characterised by the gradual decrease of *SST* (-0.02°C day^{-1}, $R^2 = 0.89$, $p < 0.05$) and an increase of *WS* (+0.02 m s^{-1} day^{-1}, $R^2 = 0.31$, $p < 0.05$) and *SWH* (+0.004 m day^{-1}, $R^2 = 0.21$, $p < 0.05$) (Fig. ~~8~~7 c, e, g). ~~The average number of consecutive days with *T* below~~Mean FDD on the ~~freezing point was 9.7, but~~freeze-up day was 501°C days and mean ϑ was 403°C days, the difference between FDD over consecutive days with $T < 1.8$°C (79°C days) and the ϑ over the entire period from the first day with $T < 1.8$°C (268°C days) suggestscaused by T oscillation around the freezing pointand melting points at the beginning of the season (Table 4).

Table 4. Conditions leading to the landfast ice freeze-up and break-up in Hornsund.

Season	Landfast ice freeze-up: Number of days with drift ice	Average ice coverage (%)	Number of consecutive days with T < -1.8 °C	FDD on the day (°C days)	θ on the day (°C days)		Thermodynamic ice thickness (m)	Number of consecutive days with T > 0°C	Landfast ice break-up: TDD on the day (°C days)	θ on the day (°C days)		Thermodynamic ice thickness (m)			
2002/03	0	NoValue		24466	195305	185	0.2737		41132	1201407	1067	0.7689			
2003/04	55	57		34766	446706	560	0.5260		2260	451631	1296	0.8597			
2004/05	72	45		6553	35530	398	0.4351		3083	701236	912	0.6983			
2005/06	101	7.6		20717	197576	389	0.4253		1280	39597	357	0.4054			
2006/07	0	NoValue		20546	167450	295	0.3646		3089	80894	565	0.5269			
2007/08	40	16		6553	35493	325	0.3849		29107	891015	696	0.5974			
2008/09	27	85		1378	7.3350	246	0.3240		30122	1051291	969	0.7285			
2009/10	24	0		0326	229		0.31		13076	0.22887		200.68	56	616	0.55
2010/11	29	48		0503	0502		3920.49		1960.42	531163		1820.80	823	0.65	
2011/12	68	11		7438	49284		1490.35		0.2422	0668		0.58	403	0.43	
2012/13	3	6.1		1557	0435		2750.45		0.3568	231163		590.80	851	0.67	
2013/14	10	9.9		0527	0503		3660.49		0.4122	0987		0.73	711	0.60	
2014/15	29	13		2527	17372		2320.41		0.31132	36728		1210.61	430	0.45	
2015/16	44	14		1634	0.9395		2060.43		0.2932	8447		200.46	213	0.30	
2016/17	6	16		22618	160412		2650.44		0.3458	16825		510.66	546	0.51	

2017/18	30	8.2	~~4~~309	~~20~~260	~~158~~0.34 ~~0.25~~ ~~12~~ ~~22~~ ~~557~~	~~0.~~52	804	0.65		
2018/19	18	3.8	~~7~~561	~~32~~381	~~231~~0.42	~~0.31~~77	~~21~~816	~~62~~0.65	~~531~~	~~0.51~~
2019/20	51	10	~~12~~430	~~99~~412	~~306~~0.44	~~0.37~~118	~~38~~1591	0.96~~107~~	~~1249~~	~~0.83~~
2020/21	2	14	~~24~~464	~~144~~352	~~217~~0.40	~~0.30~~65	~~28~~774	~~62~~0.63	~~470~~	~~0.47~~
2021/22	25	6.1	~~9~~410	~~68~~387	0.42~~279~~	~~0.35~~115	~~32~~1184	~~108~~0.81	~~851~~	~~0.67~~
2022/23	10	6.8	~~4~~452	~~32~~333	~~194~~0.39	~~0.28~~50	~~14~~730	0.61~~30~~	~~483~~	~~0.48~~
2023/24	3	23	~~3~~371	~~26~~325	~~202~~0.38	~~0.29~~132	~~37~~997	~~123~~0.73	~~689~~	~~0.59~~
2024/25	2	39	~~16~~415	~~94~~273	~~164~~0.35	~~0.26~~150	~~41~~652	0.57~~124~~	~~373~~	~~0.41~~
Mean	**28**	**21**	**~~9.7~~501**	**~~79~~403**	**~~268~~0.43**	**~~0.33~~89**	**~~25~~978**	**~~73~~0.71**	**~~681~~**	**~~0.57~~**

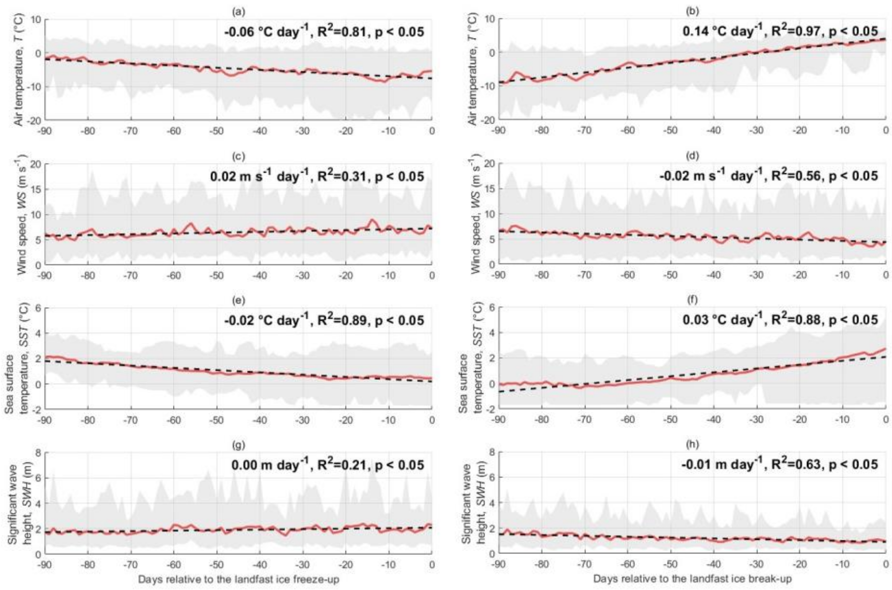

Figure ~~8~~7. Evolution of (a-b) air temperature, *T*, (c-d) wind speed, *WS*, (e-f) sea surface temperature, *SST*, and (g-h) significant wave height, *SWH*, 90 days before the landfast ice freeze-up (left side) and break-up (right side) in Hornsund over the 23 seasons from 2002-2025.

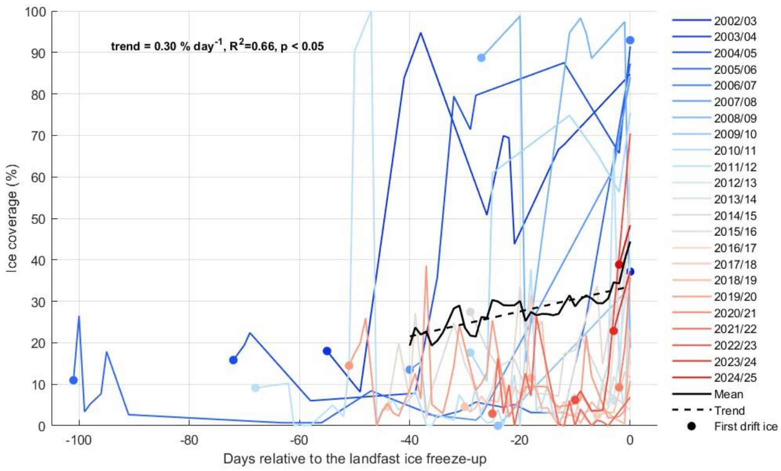

Figure ~~9~~8. Ice coverage in Hornsund from the first drift ice to the landfast ice freeze-up over the 23 seasons from 2002-2025.

In the period leading to the landfast ice break-up *T* grew gradually (+0.1°C day^{-1}, $R^2 = 0.97$, $p < 0.05$), exceeding 0°C on average 38 days before the last day with landfast ice (Fig. ~~14b). The number of consecutive days with positive *T* varied from 0 (2011/12 and 2013/14) to 53 (2010/11) with the average of 25 days, which resulted in the TDD of 73°C days on the last day with the landfast ice (Table 4).~~7b). Mean TDD on the break-up day was 89°C days (Table 4). There was also a gradual decrease in *WS* (-0.02 m s^{-1} day^{-1}, $R^2 = 0.81$, $p < 0.05$) and *SWH* (-0.01 m day^{-1}, $R^2 = 0.63$, $p < 0.05$), and an increase in *SST* (+0.03°C day^{-1}, $R^2 = 0.88$, $p < 0.05$) over 90 days leading to the landfast ice break-up (Fig. ~~8d~~7d,f,h).

— **sformatowano:** Nie Wyróżnienie

4.5 Sea ice thickness

Calculation of sea ice thickness thermodynamic growth shows a large variability between the seasons (Fig. ~~10~~9). In most seasons the ice formation started a few times with *T* oscillation around the freezing and melting points in autumn. In general, the earlier the start of ice growth the larger the maximal thickness and the longer the sea ice season. The largest thickness of 1.07~~0.96~~ m was reached in the 2019/20 season, followed by the ~~0.91~~1.03 m in the first two seasons. The smallest thickness was observed in 2015/16 (0.~~37~~51 m) and 2011/12 (0.~~46~~60 m). For ~~seven~~ten seasons the calculated thickness on August 31st was still positive despite the latest landfast ice break-up on July 20th (Fig. ~~10~~9). The estimated ice thickness on the day when we visually established the landfast ice freeze-up in the SAR imagery and the binary maps averaged 0.~~33~~43 m ranging from 0.~~22~~31 to 0.~~52~~60 m, and on the landfast ice break-up it was on average 0.~~57~~71 m with the range of 0.~~30~~46-0.~~85~~97 m (Table 4).

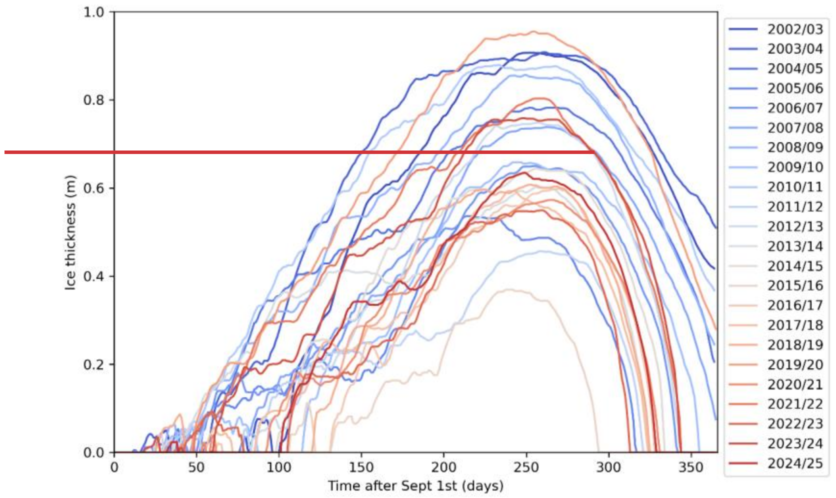

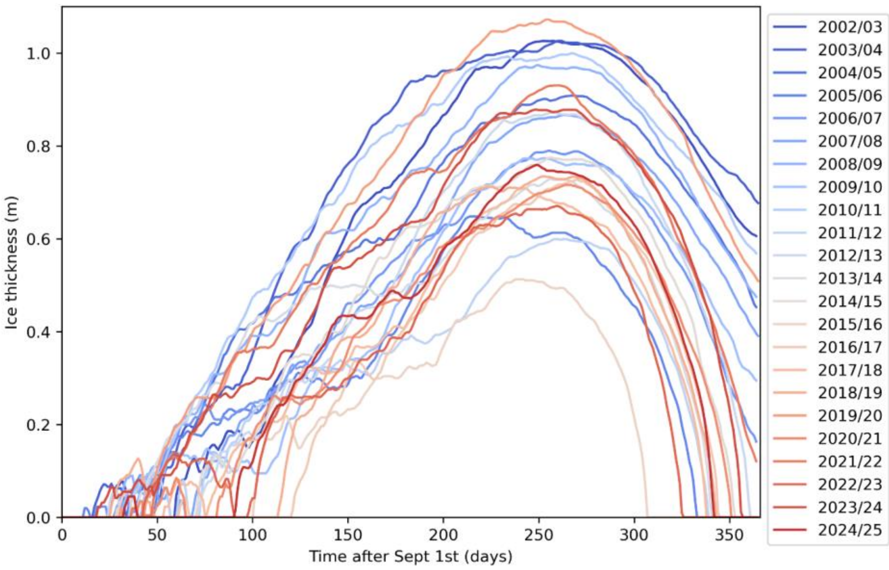

Figure ~~10~~9. Time series of sea ice thickness in Hornsund calculated using the method of Su and Wang (2012) for the 23 seasons from 2002-2025.

5 Discussion

This study is the third of a series of articles that focus on sea ice conditions in the Hornsund fjord, Svalbard. The first publication (Swirad et al., 2024a) adapted a semi-automated method of Cristea et al. (2020) and Johansson et al. (2020) to create high-resolution (50 m) near-daily binary maps of ice and open water of Hornsund using the full Sentinel-1A/B archive available at the time. The main findings included (1) a large interannual variability in sea ice conditions without a clear trend over the nine analysed seasons, (2) differences in timing and extent of the ice cover in different parts of the fjord, notably the main basin and the inner bays, and (3) a presence of a secondary peak in ice coverage in the bays in autumn, that the authors attributed to the presence of glacier ice (Swirad et al., 2024a). The second study (Swirad et al., 2026b) expanded the dataset back in time to include the full RADARSAT-2 archive and developed a method to separate the ice into glacier ice, drift ice and landfast ice. The authors showed that the ice in Hornsund was 53% drift, 35% landfast, 8.5% glacier ice, while the remaining 3.5% was either unclassified or masked out. Statistically-significant negative ~~relationships~~correlations were found between winter (January-March) water temperature and the length of the sea ice and landfast ice seasons, and between winter air temperature and the mean coverage of sea ice (drift and landfast ice combined) and landfast ice. Glacier ice coverage was negatively correlated with summer air and autumn water temperatures. At the 12-season scale no long-term trends in ice conditions were detected (Swirad et al. 2026b). In this study we further extended the dataset in time – backward by using the full Envisat ASAR archive (Papin et al., 2025a) and forward by using subsequent Sentinel-1A imagery (Papin et al., 2025b). We supplemented the dataset with meteorological data from the PPS monitoring programme, and oceanographic data from ERA5 reanalysis for a location outside the fjord. Because of the strong (R^2 = 0.95-0.96) statistically-significant ($p < 0.05$) relationships between the extent of drift ice from Swirad et al. (2026b) and our ice extent in the main basin for both the sea ice and the landfast ice seasons, as well as between the landfast ice from Swirad et al. (2026b) and our ice extent in the bays (Fig. ~~11~~10), we treat the differences between the main basin vs the bays as a proxy for the differences between drift vs landfast ice.

The extended daily, 50 m dataset adds a process-oriented perspective to these earlier studies by resolving not only long-term changes, but also the timing, spatial contrasts, and sequence of ice events within the fjord. In particular, it allows us to distinguish between drift-ice variability in the exposed main basin and landfast-ice formation and persistence in the sheltered bays, and to examine how drift ice, thermal forcing, waves, and local fjord geometry interact during freeze-up and break-up.

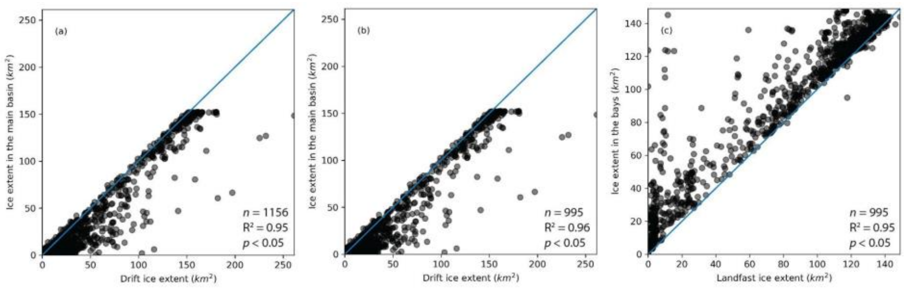

Figure ~~11~~10. Spatial extent of the drift and landfast ice in Hornsund from Swirad et al. (2026b) and the ice extent in the main basin and the bays from our study on individual days between 2012-01-02 and 2023-06-29. Panel (a) represents the sea ice season and panels (b-c) – the landfast ice season.

Expanding the dataset to 23 seasons allowed us to observe the expected long-term decreasing trends in the length of ice season and in ice coverage, such as those observed in Svalbard by Onarheim et al. (2014), Dahlke et al. (2020) and Stocker et al. (2020), in Alaska by Mahoney and Einhorn (2026) and Jensen et al (2020), and in the Canadian Archipelago by Gupta et al. (2022). The trends are stronger for the sea ice season compared to the landfast ice season, and for the main basin compared to the bays (Fig. 3). This suggests that mostly the pack ice is affected, as generally in the Arctic, while the state of the landfast ice may be more affected by local conditions, such as those of sheltered bays of eastern Hornsund. Notably, the variability of season length was more dependent on the start of the season (October-March) than on its end (May-July). The start of sea ice season is associated with the arrival of pack ice from the Barents Sea, while the end represents the disappearance of landfast ice. The unstable start vs the stable end of the sea ice season further confirms that the drift ice is mostly affected. Araźny et al. (2018) observed a gradient in meteorological conditions (temperature and humidity) between the more maritime western and more continental eastern Hornsund. The Atlantification of Hornsund where the warmer and more saline ~~Atlantic Water~~AW becomes dominant over the cooler and fresher ~~Arctic Water~~ArW (Strzelewicz et al., 2021) affects mostly the outer parts of Hornsund, while the inner bays remain highly affected by glacier outflow (Korhonen et al., ~~2024).~~2024). Extended period between the first FDD and landfast ice formation was also found along the Alaskan coastline by Mahoney and Einhorn (2026), which they attribute to the warmer water temperatures in fall, equivalent to the Atlantification in Hornsund. Further indication on the positive effect of drift ice presence for landfast ice formation has also been observed in the Beaufort and Chukchi Seas (Mahoney et al, 2014). Glacier retreat, and the resulting bay deepening provides more and more sheltered conditions for the landfast ice to form and persist, with the katabatic winds, glacier ice floating in the bays and subsurface outflow further decreasing near surface water temperatures. As increased water depth is a limiting factor for landfast ice extent (Mahoney et al, 2014, Jensen et al, 2020), retreating glaciers can provide more stable and shallow water areas for ice formation. Combination of observed over the similar timescale as ours 8% increase of AW volumetric fraction per year (Strzelewicz et al., 2021) and faster glacier retreat in Hornsund compared to other parts of Svalbard (Błaszczyk et al., 2013) further highlights the increasing local contrasts between the main basin and the bays, and between drift ice and landfast ice. This contrast between the main basin and the bays is one of the clearest process-related patterns revealed by the dataset. The main basin is more directly connected to incoming drift ice, shelf conditions, Atlantification and wave exposure, whereas the inner bays are partly decoupled from these external forcings and are more strongly influenced by local sheltering, glacier freshwater input, katabatic winds and bay geometry. The stronger decline in the main basin therefore indicates a response dominated by reduced drift-ice supply and increasing exposure to open-water conditions, while the weaker response in the bays reflects the persistence of locally controlled landfast-ice formation. Similarities between our observations with those in the Canadian Archipelago (Gupta et al, 2022) and along the Alaskan coastline (Mahoney et al., 2014; Jensen et al., 2020; Mahoney and Einhorn, 2026) puts this work into a larger Arctic Ocean context.

The decline of pack ice drifting to the entrance of Hornsund from the Barents Sea was also shown by Herman et al. (2025) for the 1979-2023 ERA5 reanalysis data, though the authors pointed to a 'regime shift' after 2005 rather than a gradual change. A decline of the sea ice in Hornsund was also shown by Muckenhuber et al. (2016) on the 2000-2014 optical and SAR imagery, though they identified icy periods of 2000-2005 and 2009-2011, and non-icy periods of 2006-2008 and 2012-2014, which could alternatively suggest warmer and colder periods of ~three years. Similar trends were observed in other fjords of Svalbard. For instance, Pavlova et al. (2019) documented an abrupt change in Kongsfjorden, where 2002/2003-2004/2005 were characterised with high sea ice coverage and the subsequent 2005/2006-2015/2016 had a reduced sea ice cover, with the minimum in 2011/2012. In Isfjorden, Muckenhuber et al. (2016) documented the abrupt change starting from the 2005/2006 season and the minimum sea ice coverage in 2011/2012 and 2013/201. Finally, Johansson et al. (2020) observed a low sea ice coverage in Kongsfjorden in 2005/2006-2007/2008 and 2011/2012-2018/2019, and in Rijpfjorden in 2011/2012, 2015/2016 and 2017/2018.

Of the bays, Burgerbukta experienced the fastest decline of the ice coverage during the sea ice and landfast ice seasons, which is intuitive given its location in northern Hornsund, most exposed to the waves arriving from the south-west (Herman et al., 2019; Swirad et al., 2023b). We observed a gradual increase in air and water temperatures, particularly in autumn months (Fig. 5), which could decrease persistence (increase melting) of drift ice, as well as delay the in situ ice formation. Interestingly, there is a statistically-significant decline in winter wind speed. Wind has a complex effect on ice formation and persistence. Wind at the beginning of the sea ice season may accelerate ice production through accelerated ocean heat loss and ice deformation (Kwok, 2006). This phenomenon may become limited with decreasing wind speed, further contributing to slower in situ ice production. In the nearshore or fjord environment, cold katabatic winds from glaciers can decrease near surface water temperature in the bays enhancing the ice production. However, wind from the open sea will break up the forming landfast ice, particularly thin one at the beginning of the season.

On the top of the general trend of ice decline, there is a great variability in ice conditions from year to year that was already noticed in our previous studies (Swirad et al., 2024a; 2026b). The longest sea ice seasons and the largest ice coverage characterised the first three seasons (pre-regime shift) as well as two late seasons of 2019/20 and 2021/22. Conversely, the 2011/12 and 2013/14 remain the least icy seasons of the 21st century, while the 2015/16 was the shortest (Table 2). The seasonal ice parameters are strongly (R^2 of 0.48-0.61) correlated to T_{autumn} and T_{winter} (Fig. 6). T_{autumn} plays a major role for the length of the sea ice season and the ice coverage in the main basin during both the sea ice and landfast ice seasons, further pointing to the variability of drift ice conditions at the beginning of the season. Conversely, the length of the landfast ice season as well as the ice coverage in the bays respond mostly to T_{winter}, which is the period of landfast ice formation. Further corroborating the findings of Selyunzhenok et al. (2017) and Mahoney and Einhorn (2026) with the increase in time delay between the first FDD and landfast ice formation, *T* in the winter months through FDD widely controls ice thickness increase which then affects the time needed to melt/break-up the landfast ice at the end of the season. We found that all ice season parameters correlated better with *T* than water temperature~~.~~, which matches the findings from Gupta et al. (2022) who found a clear correlation between *T* and the landfast ice formation. This result is different from that of our previous study (Swirad et al., 2026b), in which water temperature controlled the length of the season, and air temperature - ice coverage. We ascribe this difference to the duration of the study (23 vs 12 seasons) as well as using *SST* of a point outside Hornsund (here) and ~~sea bed mooring data at 10-23 m depth (previous study). De Steur et al. (2023) found a relationship between Fram Strait ice extent and water temperature measured at 55-2440 m depths. However, no in situ water temperature data were available for the entire 2002-2025 period of this study and ERA5 reanalysis was used instead.~~seabed mooring data at 10-23 m depth (previous study). Deviation of points

— **sformatowano:** Indeks górny

— **sformatowano:** Czcionka: Nie Kursywa

— **sformatowano:** Czcionka: Nie Kursywa

— **sformatowano:** Czcionka: Nie Kursywa

— **sformatowano:** Czcionka: Nie Kursywa from the trendline in Fig. 6 suggests that *T* is not the only determinant of ice conditions. For instance, 2002/2003 had the lowest T_{winter}, but did not have the highest ice coverage. Similarly, 2011/2012, 2013/2014 and 2015/2016 all had the highest T_{winter}, but 2015/2016 had a considerably shorter landfast ice season (Fig. 6). Additionally, the meteorological station at PPS does not fully represent thermal conditions across the whole fjord (Araźny et al., 2018).

Multiple linear regression showed that combining multiple parameters allows a better fit (R^2 of 0.73-0.92) between the environmental and the eight ice season parameters than using a single variable (~~Fig. 7~~Table 3). T_{autumn} and T_{winter} were still the most important, but other parameters were also included (Table 3). The impact of *SST* was similar though weaker than ~~the air temperature.~~*T*. For six ice parameters, WS_{summer} was important, showing a negative correlation, though the physical meaning seems unclear. The positive relationship between WS_{autumn} and the length of the sea ice season supports the acceleration of ice production through deformation (Kwok, 2006). We did not find any negative relationships between WS_{spring} and/or SWH_{spring} and ice season parameters to support the hypothesis of faster landfast ice break-up and melting by wind waves (Graham et al., 2019). *SWH* was generally the least important factor, which we justify by wave transformation at the entrance and inside the fjord which prevents direct comparison between the value from a single point outside the fjord and ice conditions in the fjord itself. However, when present, the relationship was negative which supports that waves break ice contributing to the shortening of the season and decrease of ice extent (Table 3). Long-term monitoring of water temperature and wave parameters could allow for more direct relationships to be identified. An alternative approach to describing environmental conditions, rather than using fixed 3-month seasonal averages, could be explored to improve model fit (Lei et al., 2012).

We also observed a temporal shift in ice phenomena over the years. The first seasons (pre-regime shift, i.e. until 2005) were characterised by a rapid increase in ice coverage between December and January, later it was from January to February, and in some years from February to March (Fig. S3 in the Supplement). This is similar to the observations by Mahoney and Einhorn (2026) for the Alaskan coastline. In consequence, Hornsund shores are more exposed to storm waves, and the hazard of coastal flooding and erosion is higher. Zagórski et al. (2015) pointed to autumn as a season of limited ice cover and large waves. However, our results suggest that December-February may be critical months, both because it is the season with the most intense storms (Swirad et al., 2023b) and because it experiences significant ice decline. Glacier calving and glacier ice accumulation in the bays, despite glacier retreat between June and October-December (Błaszczyk et al., 2023), may not level this shift. Glacier ice tends to be spread or grouped in belts, and it does not attenuate wave energy as efficiently as sea ice; it may also serve as abrasive tool, e.g. when moving up and down the shore with waves (Swirad et al., 2026a). Swirad et al. (2026b) observed a negative correlation between glacier ice coverage and both the glacier calving (approximated by the increase of annual land mask) and the summer air and autumn water temperatures, which suggests that although fewer growlers and bergy bits are expelled from glacier fronts during cold summers/autumns, they persist in the fjord for longer. Li et al. (2025) observed that for southern Svalbard the peak in air temperature occurred in late June, followed by a peak in water temperatures in August and a peak in glacier retreat in September, showing a clear trend between the water temperatures and the glacier retreats.

— sformatowano: Czcionka: Arial, 11 pkt, Ligatury: Standardowe + Kontekstowe

— sformatowano: Czcionka: Nie Kursywa

— sformatowano: Czcionka: Nie Kursywa

— sformatowano: Czcionka: Nie Kursywa

— sformatowano: Czcionka: Nie Kursywa

— sformatowano: Czcionka: Nie Kursywa

— sformatowano: Czcionka: Nie Kursywa

— sformatowano: Czcionka: Arial, 11 pkt, Ligatury: Standardowe + Kontekstowe

Suitable conditions for the landfast ice formation include the presence of drift ice (Figs. 4 and 98) that attenuates waves and lowers near-surface water temperature, and extended period of cold air temperatures. As temperatures may return to the melting point a few times before the landfast ice onset, ϑ, the cumulative effect of FDD and TDD starting from the first day below -1.8°C, seems to better reflect conditions necessary for water freezing than FDD alone. This is corroborated by finding along the number of consecutive days with negative temperatures or TDD over these (both can be 0).Alaskan coastline by Mahoney and Einhorn (2026) that in their 27-year data record (1996-2023) found a delay in time between the first FDD and landfast ice formation. The minimal ϑ on the day of the landfast ice freeze-up was 130229°C days (Table 4). The ice thickness calculated in thermodynamic terms (Lebedev, 1938) for the landfast ice freeze-up day was on average 0.3343 m, which may indicate a minimum thickness needed for ice detection using C-band SAR imagery. New SAR missions, the recently launched NISAR (NASA-ISRO) mission and upcoming ROSE-L (ESA), are carrying the L-band sensors with the free and open data policy, and in early March 2026 there were already approx. 180 NISAR images collected over Hornsund. Wakabayashi et al. (2004) showed a relationship between the L-band SAR backscatter values and sea ice thickness from approx. 5-10 cm thickness. For earlier years, it is possible that the landfast ice onset could be visible on SAR imagery earlier but the lower temporal resolution of Envisat ASAR imagery resulted in a less accurate start date for the freeze-up. However, the seasons with the largest data gap before the landfast ice onset represented both thinner (2009/10, 2002/03) and thicker (2003/04) than average ice (Table 5). The daily temporal resolution also clarifies the sequence of processes leading to freeze-up. Drift ice typically appears before landfast ice forms and may precondition freeze-up by reducing wave exposure and cooling near-surface waters. Stable landfast ice then initiates preferentially in sheltered bays, where local topography and reduced exposure favour persistence. The effect of local conditions on fast ice formation were also observed by Gupta et al. (2022) in the Canadian Archipelago. Conversely, break-up occurs after drift ice has disappeared from the fjord, leaving the remaining landfast ice increasingly exposed to positive air temperatures and suggesting that mechanical forcing from waves and locally generated wind seas may contribute to final break-up.

Table 5. Dates and number of days with no data before/after the landfast ice freeze-up/break-up in Hornsund.

Season	Number of days with no data before landfast ice freeze-up	Number of days with no data after landfast ice break-up
2002/03	36	0
2003/04	11	39
2004/05	1	7
2005/06	7	8
2006/07	8	3
2007/08	2	1
2008/09	0	0
2009/10	23	2
2010/11	1	1
2011/12	0	0
2012/13	2	2
2013/14	0	0
2014/15	1	2
2015/16	4	3
2016/17	0	1
2017/18	0	0
2018/19	0	0
2019/20	0	0
2020/21	0	0

sformatowano: Czcionka: Arial, 11 pkt, Ligatury: Standardowe + Kontekstowe

Tabela sformatowana

Season	Number of days with no data before landfast ice freeze-up	Number of days with no data after landfast ice break-up
2002/03	36	0
2003/04	11	39
2021/22	3	5
2022/23	3	1
2023/24	2	0
2024/25	1	0

Tabela sformatowana

Notably, calculating ice thickness using Eqs. 3 and 4 involves several assumptions and limitations which need to be taken into account when interpreting the results. For instance, these equations do not account for oceanic heat flux, assume a linear vertical ice-temperature profile, and ignore snow-cover effects. The present calculations are, therefore, only an estimate intended to highlight the importance of other processes. The landfast ice break-up coincided with the time when pack ice was already absent (Fig. 98) and temperatures remained over the melting point for ca. 25 days. Interestingly both 9 and thermodynamic ice thickness remained positive which may suggest that other processes play a key role in ice break-up. We suggest that these are waves, both swell/sea from the south-west and those locally generated by wind, that break the edges of the landfast ice and accelerate melting (Graham et al., 2019). The thermodynamic ice thickness at the time of the landfast ice break-up averaged 0.5771 m. In situ ice ice thickness measurements, as well as local meteorological stations and moorings in the individual bays of Hornsund would help prove this hypothesis, enabling to account for local-scale differences in meteorological and oceanographic conditions, given the east-west gradient (Araźny et al., 2018) and topographic complexity.

sformatowano: Czcionka: Arial, 11 pkt, Ligatury: Standardowe + Kontekstowe

6 Conclusions

The full archive of high-resolution SAR imagery (Envisat ASAR, RADARSAT-2 and Sentinel-1) fully covering Hornsund fjord between October 2002 and August 2025 was used to create an unprecedented set of near-daily binary ice/open water maps over the fjord area for 23 seasons. We observed a general trend of sea ice season shortening by 2.3 days yr^{-1}, and a gradual decrease in average ice coverage during the sea ice season, particularly in the main basin of Hornsund (-1.6% yr^{-1}), which we attributed to the general decrease in pack ice duration and extend in the Arctic. The changes are smaller down to negligible for the landfast ice season and the inner bays of the fjord, where landfast ice develops in situ. On the top of the longer-term trend, the results suggest a great interannual variability in ice conditions, which are strongly related to the autumn (October-December) and/or winter (January-March) air temperatures averaged from the observations at the Polish Polar Station. The length of the sea ice season is shortened by 19.5 days for every 1°C increase in the mean autumn air temperature (R^2 = 0.61, $p < 0.05$). Step-wise multiple linear regression showed that predicting ice conditions can be improved by combining a range of meteorological and oceanographic parameters (air temperature, *T*, wind speed, *WS*, sea surface temperature, *SST* and significant wave height, *SWH*) with *SST* having a similar but more subtle effect than *T*, higher autumn *WS* characterising longer ice seasons and *SWH* showing weak but negative correlation with the ice conditions.

In the period leading to the landfast ice freeze-up, *T* typically remained under the freezing point (-1.8°C) for over 90 days, decreasing gradually by -0.1°C day^{-1}. At that time, the drift ice was present in the fjord, lowering the near surface water temperature and protecting fjord waters from the incoming wave energy. In average, for 40 days prior to the landfast ice formation the ice coverage exceeded 20%, rising to 26% on the day preceding the freeze-up. The landfast ice break-up was characterised by a lack of drift ice and positive *T* for an average of 38 days with a gradual increase of 0.1°C day^{-1} over the 90-day period. Calculation of the sea ice thickness in thermodynamic terms showed that the landfast ice is detectable on C-band SAR imagery when it is thicker than 0.3343 m (range: 0.2231-0.5260 m) while the landfast ice break-up is related to other processes than only melting (such as breaking by waves) since on the date identified as the landfast ice season end the thermodynamic thickness averaged 0.5771 m.

This study provides open long-term (23 seasons) high spatial (50 m) and temporal (2 days) resolution dataset of ice maps for any analyses including fjord hydrography, glacier/ocean interaction and ecology. It can help assess wave impact on coastal change and safety for boat and snowmobile operations. Finally, because of its duration and detail, it provides information on the changing climate of the Arctic and the impact of weather and oceanic conditions on the state of ice.

Data availability

The binary ice/open water maps are available in the PANGAEA repository: those based on Envisat ASAR 2002-2012 are at https://doi.org/10.1594/PANGAEA.986427 (Papin et al., 2025a), those based on RADARSAT-2 2012-2016 are at https://doi.pangaea.de/10.1594/PANGAEA.969031 (Swirad et al., 2024b), those based of Sentinel-1A/B 2014-2023 are at https://doi.org/10.1594/PANGAEA.963167 (Swirad et al., 2023a), and those based on Sentinel-1A 2023-2025 are at https://doi.org/10.1594/PANGAEA.987853 (Papin et al., 2025b). Additionally, three erroneously classified images from Swirad et al. (2023a) are available at https://doi.org/10.5281/zenodo.17350297 (Swirad, 2025).

Supplement

Table S1 in the Supplement is the time series of the extent and coverage of ice in Hornsund and its parts. Table S2 in the Supplement is a time series of meteorological and oceanographic conditions. Table S3 in the Supplement is a summary of ice and climate parameters for individual seasons. Document S4 contains supplementary figures.

Author contribution

ZMS and AMJ conceptualised the study. EM pre-processed the SAR scenes. VP processed and analysed the data with the help from ZS. VP and ZS wrote the original manuscript. All authors edited the manuscript and agreed on its final version.

Competing interests

None of the authors has any competing interests.

Acknowledgements

We thank Meri Korhonen (IG PAS) for preparing meteorological data. Envisat ASAR and Sentinel-1 data are freely available through the European Union's Earth observation Copernicus programme (https://copernicus.eu, last access: 21 July 2025). RADARSAT-2 data was provided by NCS/KSAT under the Norwegian-Canadian RADARSAT-2 agreement 2011–16. ERA5 data are freely available at the Climate Data Store website (https://cds.climate.copernicus.eu/, last access: 17 November 2025).

Financial support

This study was funded by the European Space Agency (HIRLOMAP ESA Contract No. 4000146036/24/I-DT-bgh). Vincent Papin's stay at IG PAS was partly funded by the European Union's Erasmus programme. Eirik Malnes was partly funded by the European Space Agency (Svalbard Cryosphere Digital Twin - SvalbardDT, ESA Contract No. 4000146232/24/I-KE).

Bibliography

Araźny, A., Przybylak, R., Wyszyński, P., Wawrzyniak, T., Nawrot, A., and Budzik, T.: Spatial variations in air temperature and humidity over Hornsund fjord (Spitsbergen) from 1 July 2014 to 30 June 2015, Geografiska Annaler Series a Physical Geography, 100, 27–43, https://doi.org/10.1080/04353676.2017.1368832, ~~2017~~2018.

~~Barzycka, B., Grabiec, M., Błaszczyk, M., Ignatiuk, D., Laska, M., Hagen, J. O., Jania, J.: Changes of glacier facies on Hornsund glaciers (Svalbard) during the decade 2007–2017, Remote Sensing of Environment, 251, 112060, https://doi.org/10.1016/j.rse.2020.112060, 2020.~~

Błaszczyk, M., Jania, J. A., and Kolondra, L.: Fluctuations of tidewater glaciers in Hornsund fjord (southern Svalbard) since the beginning of the 20th century, Polish Polar Research, 34(4), 327–352, https://journals.pan.pl/dlibra/publication/114504/edition/99557/content (last access: 24 March 2026), 2013.

Błaszczyk, M., Ignatiuk, D., Uszczyk, A., Cielecka-Nowak, K., Grabiec, M., Jania, J. A., Moskalik, M., and Walczowski, W.: Freshwater input to the Arctic fjord Hornsund (Svalbard), Polar Research, 38, https://doi.org/10.33265/polar.v38.3506, 2019.

Błaszczyk, M., Moskalik, M., Grabiec, M., Jania, J., Walczowski, W., Wawrzyniak, T., Strzelewicz, A., Malnes, E., Lauknes, T. R., and Pfeffer, W. T.: The response of tidewater glacier Termini positions in Hornsund (Svalbard) to climate forcing, 1992–2020, Journal of Geophysical Research Earth Surface, 128, https://doi.org/10.1029/2022jf006911, 2023.

van den Broek, D., Urbancic, G.H.,Rantanen, M., and Vihma, T.: Svalbard's record-breaking arctic summer 2024: Anomalies beyond climatological warming trends, Geophysical ResearchLetters, 52, e2025GL115015, https://doi.org/10.1029/2025GL115015, 2025.

Casas-Prat, M. and Wang, X. L.: Projections of extreme ocean waves in the Arctic and potential implications for coastal inundation and erosion, J. Geophys. Res. Oceans, 125, e2019JC015745, https://doi.org/10.1029/2019JC015745, 2020.

Cottier, F. R., Nilsen, F., Skogseth, R., Tverberg, V., Skarðhamar, J., and Svendsen, H.: Arctic fjords: a review of the oceanographic environment and dominant physical processes, Geological Society London Special Publications, 344, 35–50, https://doi.org/10.1144/sp344.4, 2010.

Cristea, A., Van Houtte, J., and Doulgeris, A. P.: Integrating incidence angle dependencies into the Clustering-Based Segmentation of SAR images, IEEE Journal of Selected Topics in Applied Earth Observations and Remote Sensing, 13, 2925–2939, https://doi.org/10.1109/jstars.2020.2993067, 2020.

Dahlke, S., Hughes, N., Wagner, P, Gerland, S., Wawrzyniak, T., Ivanov, B., and Maturilli, M.: The observed recent surface air temperature development across Svalbard and concurring footprints in local sea ice cover, Int. J. Climatol., 40, 5246–5265, https://doi.org/10.1002/joc.6517, 2020.

Dobiński, W. and Kasprzak, M.: Permafrost base degradation: characteristics and unknown thread with specific example from Hornsund, Svalbard, Frontiers in Earth Science, 10, https://doi.org/10.3389/feart.2022.802157, 2022.

Dong, Y., Xiao, P., Zhang, X. Ge, D., Yu, J., Chen, Y., Wu, Q., Ma, Y., Liu, R., Luan, W., Liu, H., and Bai, J.: Increased vulnerability of Arctic potential ice roads under climate change, Commun Earth Environ, 6, 37, https://doi.org/10.1038/s43247-025-02011-y, 2025.

Frank, L., Jonassen, M. O., Skogseth, R., and Vihma, T.: Atmospheric climatologies over Isfjorden, Svalbard, Journal of Geophysical Research Atmospheres, 128, https://doi.org/10.1029/2022jd038011, 2023.

Fraser N. J., Skogseth R., Nilsen F., and Inall M. E.: Circulation and exchange in a broad Arctic fjord using glider-based observations, Polar Research, 37, 1485417, https://doi.org/10.1080/17518369.2018.1485417, 2018.

Graham, R. M., Itkin, P., Meyer, A., Sundfjord, A., Spreen, G., Smedsrud, L. H., Liston, G. E., Cheng, B., Cohen, L., Divine, D., Fer, I., Fransson, A., Gerland, S., Haapala, J., Hudson, S. R, Johansson, A. M., King, J., Merkouriadi, I., Peterson, A. K., Provost, C., Randelhoff, A., Rinke, A., Rösel, A., Sennéchael, N., Walden, V. P., Duarte, P., Assmy, P., Steen, H. and Granskog, M. A.: Winter storms accelerate the demise of sea ice in the Atlantic sector of the Arctic Ocean, Scientific Reports, 9, 9222, https://doi.org/10.1038/s41598-019-45574-5, 2019.

Gupta, K., Mukhopadhyay, A., Babb, D. G., Barber, D. G., and Ehn, J. K.: Landfast sea ice in Hudson Bay and James Bay: Annual cycle, variability and trends, 2000–2019, Elementa Science of the Anthropocene, , 10(1), 00073, https://doi.org/10.1525/elementa.2021.00073, 2022.

Herman, A., Swirad, Z. M., and Moskalik, M.: Increased exposure of the shores of Hornsund (Svalbard) to wave action due to a rapid shift in sea ice conditions, Elementa Science of the Anthropocene, 13, https://doi.org/10.1525/elementa.2024.00067, 2025.

Herman, A., Wojtysiak, K., and Moskalik, M.: Wind wave variability in Hornsund fjord, west Spitsbergen, Estuar. Coast. Shelf S., 217, 96–109, https://doi.org/10.1016/j.ecss.2018.11.001, 2019.

Hersbach, H., Bell, B., Berrisford, P., Biavati, G., Horányi, A., Muñoz Sabater, J., Nicolas, J., Peubey, C., Radu, R., Rozum, I., Schepers, D., Simmons, A., Soci, C., Dee, D., and Thépaut, J.-N.: ERA5 hourly data on single levels from 1940 to present, Copernicus Climate Change Service Climate Data Store (CDS), https://doi.org/10.24381/cds.adbb2d47, 2023 (last access: 8 October 2025).

IPCC: Climate Change 2023: Synthesis Report. Contribution of Working Groups I, II and III to the Sixth Assessment Report of the Intergovernmental Panel on Climate Change [Core Writing Team, H. Lee and J. Romero (eds.)]. IPCC, Geneva, Switzerland, 184 pp., doi: 10.59327/IPCC/AR6-9789291691647, 2023.

Itkin, P., Losch, M., and Gerdes, R.: Landfast ice affects the stability of the Arctic halocline: Evidence from a numerical model, Journal of Geophysical Research Oceans, 120, 2622–2635, https://doi.org/10.1002/2014jc010353, 2015.

Jakacki, J., Przyborska, A., Kosecki, S., Sundfjord, A., and Albretsen, J.: Modelling of the Svalbard fjord Hornsund, Oceanologia, 59, 473–495, https://doi.org/10.1016/j.oceano.2017.04.004, 2017.

Jansen, E., Christensen, J. H., Dokken, T., Nisancioglu, K. H., Vinther, B. M., Capron, E., Guo, C., Jensen, M. F., Langen, P. L., Pedersen, R. A., Yang, S., Bentsen, M., Kjær, H. A., Sadatzki, H., Sessford, E., and Stendel, M.: Past perspectives on the present era of abrupt Arctic climate change, Nature Climate Change, 10, 714–721, https://doi.org/10.1038/s41558-020-0860-7, 2020.

Jensen, D., Mahoney, A., and Resler, L.: The annual cycle of landfast ice in the eastern Bering Sea, Cold Regions Science and Technology, 14, 103059, https://doi.org/10.1016/j.coldregions.2020.103059, 2020.

Larsen, Y., Engen, G., Lauknes, T., Malnes, E., and Høgda, K.: A generic differential interferometric SAR processing system, with applications to land subsidence and snow-water equivalent retrieval, Fringe 2005 Workshop, 610, ISBN 92-9092-921-9, 2006.

Lei, R., Leppäranta, M., Cheng, B., Heil, P., and Li, Z.: Changes in ice-season characteristics of a European Arctic lake from 1964 to 2008, Climatic Change, 115, 725–739, https://doi.org/10.1007/s10584-012-0489-2, 2012.

Johansson, A. M., Malnes, E., Gerland, S., Cristea, A., Doulgeris, A. P., Divine, D. V., Pavlova, O., and Lauknes, T. R.: Consistent ice and open water classification combining historical synthetic aperture radar satellite images from ERS-1/2, Envisat ASAR, RADARSAT-2 and Sentinel-1A/B, Annals of Glaciology, 61, 40–50, https://doi.org/10.1017/aog.2019.52, 2020.

Korhonen, M., Moskalik, M., Głowacki, O., and Jain, V.: Oceanographic monitoring in Hornsund fjord, Svalbard, Earth System Science Data, 16, 4511–4527, https://doi.org/10.5194/essd-16-4511-2024, 2024.

Kowalik, Z., Marchenko, A., Brazhnikov, D., and Marchenko, N.: Tidal currents in the western Svalbard Fjords, Oceanologia, 57, 318–327, https://doi.org/10.1016/j.oceano.2015.06.003, 2015.

Kwok, R.: Contrasts in sea ice deformation and production in the Arctic seasonal and perennial ice zones,J. Geophys. Res., 111, C11S22, https://doi.org/10.1029/2005JC003246, 2006.

Lebedev, V.: Rost l'da v arkticheskikh rekakh i moriakh v zavisimosti ot otritsatel'nykh temperatur vozdukha, Problemy Arktiki, 5(6), 9–25, 1938.

Li, T., Hofer, S., Moholdt, G. Igneczi, A., Heidler, K., Zhu, X. X., and Bamber, J.: Pervasive glacier retreats across Svalbard from 1985 to 2023, Nat Commun 16, 705, https://doi.org/10.1038/s41467-025-55948-1, 2025.

Mahoney, A. R., and Einhorn, A. H.: The Evolving Decline of Landfast Sea Ice in Northern Alaska and Adjacent Waters: Results from an Updated Climatology, Journal of Geophysical Research: Oceans, 131(1), e2025JC022464, https://doi.org/10.1029/2025JC022464, 2026.

Mahoney, A. R., Eicken, H., Gaylord, A. G., and Gens, R.: Landfast sea ice extent in the Chukchi and Beaufort Seas: The annual cycle and decadal variability, Cold Regions Science and Technology, 103, 41–56, https://doi.org/10.1016/j.coldregions.2014.03.003. 2014.

— sformatowano: Norweski (Bokmål)

Mioduszewski, J., Vavrus, S., and Wang, M.: Diminishing Arctic Sea ice promotes stronger surface winds, Journal of Climate, 31, 8101–8119, https://doi.org/10.1175/jcli-d-18-0109.1, 2018.

Muckenhuber, S., Nilsen, F., Korosov, A., and Sandven, S.: Sea ice cover in Isfjorden and Hornsund, Svalbard (2000–2014) from remote sensing data, The Cryosphere, 10, 149–158, https://doi.org/10.5194/tc-10-149-2016, 2016.

NOAA: National Centers for Environmental Information, Climate at a Glance: Global Time Series, https://www.ncdc.noaa.gov/cag/, last access: 15 June 2025.

NPI: Kartdata Svalbard 1:100 000 (S100 Kartdata)/Map Data, Norwegian Polar Institute [data set], https://doi.org/10.21334/npolar.2014.645336c7, 2014.

Onarheim, I. H., Smedsrud, L. H., Ingvaldsen, R. B., and Nilsen, F.: Loss of sea ice during winter north of Svalbard, Tellus, 66A, 23933, https://doi.org/10.3402/tellusa.v66.23933, 2014.

Papin, V., Swirad, Z. M., Johansson, A. M., and Malnes, E.: Ice distribution in Hornsund fjord, Svalbard from Envisat ASAR (2002–2012), PANGAEA [data set], https://doi.org/10.1594/pangaea.986427, 2025a.

Papin, V., Swirad, Z. M., Johansson, A. M., and Malnes, E.: Ice distribution in Hornsund fjord, Svalbard from Sentinel-1A (2023–2025), PANGAEA [data set], https://doi.org/10.1594/PANGAEA.987853, 2025b.

Park, J.-W., Korosov, A. A., Babiker, M., Won, J.-S., Hansen, M. W., and Kim, H.-C.: Classification of sea ice types in Sentinel-1 synthetic aperture radar images, The Cryosphere, 14, 2629–2645, https://doi.org/10.5194/tc-14-2629-2020, 2020.

Pizzolato, L., Howell, S. E. L., Dawson, J., Laliberté, F., and Copland, L.: The influence of declining sea ice on shipping activity in the Canadian Arctic, Geophysical Research Letters, 43, https://doi.org/10.1002/2016gl071489, 2016.

Pavlova, O., Gerland, S., and Hop, H.: Changes in sea ice extent and thickness in Kongsfjorden, Svalbard (2003–2016), in: The Ecosystem of Kongsfjorden, Svalbard, edited by: Hop, H. and Wiencke, C., Advances in Polar Ecology, 2, Springer, Cham, 105–136, https://doi.org/10.1007/978-3-319-46425-1_4, 2019.

Promińska, A., Falck, E., and Walczowski, W.: Interannual variability in hydrography and water mass distribution in Hornsund, an Arctic fjord in Svalbard, Polar Research, 37, 1495546, https://doi.org/10.1080/17518369.2018.1495546, 2018.

Rinke, A., Maturilli, M., Graham, R. M., Matthes, H., Handorf, D., Cohen, L., Hudson, S. R., and Moore, J. C.: Extreme cyclone events in the Arctic: Wintertime variability and trends, Environmental Research Letters, 12, 094006, https://doi.org/10.1088/1748-9326/aa7def, 2017.

Shulman, I., Jarosz, E., Cayula, S., and Metzger, E. J.: Dynamics of the Polar Front in the southwestern area of Svalbard, Norway, Ocean Dynamics, 74(8), 637–653, https://doi.org/10.1007/s10236-024-01624-9, 2024.

Smith, L. C. and Stephenson, S. R.: New Trans-Arctic shipping routes navigable by midcentury, Proceedings of the National Academy of Sciences, 110, E1191-5, https://doi.org/10.1073/pnas.1214212110, 2013.

de Steur, L., Sumata, H., Divine, D. V., Granskog, M. A., and Pavlova O.: Upper ocean warming and sea ice reduction in the East Greenland Current from 2003 to 2019, Commun. Earth Environ., 4, 261, https://doi.org/10.1038/s43247-023-00913-3, 2023.

Selyuzhenok , V., Mahoney , A., Krumpen , T., Castellani , G., & Gerdes , R.: Mechanisms of fast-ice development in the south-eastern Laptev Sea: a case study for winter of 2007/08 and 2009/10, Polar Research, 36, 1411140, https://doi.org/10.1080/17518369.2017, 1411140, 2017.

Stocker, A. N., Renner, A. H. H., and Knol-Kauffman, M.: Sea ice variability and maritime activity around Svalbard in the period 2012–2019, Scientific Reports, 10, 17043, https://doi.org/10.1038/s41598-020-74064-2, 2020.

Strzelewicz, A., Przyborska, A., and Walczowski, W.: Increased presence of Atlantic Water on the shelf south-west of Spitsbergen with implications for the Arctic fjord Hornsund, Progress in Oceanography, 200, 102714, https://doi.org/10.1016/j.pocean.2021.102714, 2021.

Su, H., and Y. Wang: Using MODIS data to estimate sea ice thickness in the Bohai Sea (China) in the 2009–2010 winter, J. Geophys. Res., 117, C10018, https://doi.org/10.1029/2012JC008251, 2012.

Svendsen, H., Beszczynska-Møller, A., Hagen, J. O., Lefauconnier, B., Tverberg, V., Gerland, S., Ørbæk, J. B., Bischof, K., Papucci, C., Zajaczkowski, M., Azzolini, R., Bruland, O., and Wiencke, C.: The physical environment of Kongsfjorden–Krossfjorden, an Arctic fjord system in Svalbard, Polar Research, 21, 133–166, https://doi.org/10.3402/polar.v21i1.6479, 2002.

Swerpel, S.: The Hornsund Fiord: water masses, Polish Polar Research, 6(4), https://journals.pan.pl/Content/111444 (last access: 24 March 2026), 1985.

Swirad, Z. M.: Correction to the “Ice distribution in Hornsund fjord, Svalbard from Sentinel-1A/B (2014–2023)” dataset, Zenodo [data set], https://doi.org/10.5281/zenodo.17350297, 2025.

Swirad, Z. M., Johansson, A. M., and Malnes, E.: Ice distribution in Hornsund fjord, Svalbard from Sentinel-1A/B (2014–2023), PANGAEA [data set], https://doi.org/10.1594/PANGAEA.963167, 2023a.

Swirad, Z. M., Moskalik, M., and Herman, A.: Wind wave and water level dataset for Hornsund, Svalbard (2013–2021), Earth System Science Data, 15(6), 2623–2633, https://doi.org/10.5194/essd-15-2623-2023, 2023b.

Swirad, Z. M., Johansson, A. M., and Malnes, E.: Extent, duration and timing of the sea ice cover in Hornsund, Svalbard, from 2014–2023, The Cryosphere, 18(2), 895–910, https://doi.org/10.5194/tc-18-895-2024, 2024a.

Swirad, Z. M., Johansson, A. M., and Malnes, E.: Ice distribution in Hornsund fjord, Svalbard from RADARSAT-2 (2012–2016), PANGAEA [data set], https://doi.org/10.1594/PANGAEA.969031, 2024b.

Swirad Z. M., Herman A., and Moskalik M.: Sub-monthly to inter-annual Arctic gravel beach change and controlling factors, EGU General Assembly 2026, Vienna, Austria, 3–8 May 2026, EGU26-2311, https://doi.org/10.5194/egusphere-egu26-2311, 2026a.

Swirad, Z. M., Johansson, A. M., and Malnes, E.: Distribution of landfast, drift and glacier ice in Hornsund, Svalbard, The Cryosphere, 20, 113–134, https://doi.org/10.5194/tc-20-113-2026, 2026b.

Wakabayashi, H., Matsuoka, T., Nakamura, K., and Nishio, F.: Polarimetric Characteristics of sea ice in the sea of Okhotsk observed by airborne L-band SAR, IEEE Transactions on Geoscience and Remote Sensing, 42(11), 2412–2425, https://doi.org/10.1109/TGRS.2004.836259, ~~2024~~2004.

Wawrzyniak, T. and Osuch, M.: A 40-year High Arctic climatological dataset of the Polish Polar Station Hornsund (SW Spitsbergen, Svalbard), Earth System Science Data, 12, 805–815, https://doi.org/10.5194/essd-12-805-2020, 2020.

Wojtysiak, K., Herman, A., and Moskalik, M.: Wind wave climate of west Spitsbergen: seasonal variability and extreme events, Oceanologia, 60, 331–343, https://doi.org/10.1016/j.oceano.2018.01.002, 2018.

Zagórski, P., Rodzik, J., Moskalik, M., Strzelecki, M. C., Lim, M., Błaszczyk, M., Promińska, A., Kruszewski, G., Styszyńska, A., and Malczewski, A.: Multidecadal (1960–2011) shoreline changes in Isbjørnhamna

(Hornsund, Svalbard), Polish Polar Research, 36(4), 369–390, https://journals.pan.pl/Content/99617 (last access: 24 March 2026), 2015.

Zakhvatkina, N., Korosov, A., Muckenhuber, S., Sandven, S., and Babiker, M.: Operational algorithm for ice–water classification on dual-polarized RADARSAT-2 images, The Cryosphere, 11, 33–46, https://doi.org/10.5194/tc-11-33-2017, 2017.

Sformatowano: Do lewej, Interlinia: Wielokrotne 1,15 wrs

— sformatowano: Czcionka: Arial, Nie Pogrubienie,